

Numerical Modelling of Cavitation

Benoît POUFFARY

CNES – Launcher Directorate
Rond Point de l'Espace
91023 Evry Cedex
FRANCE

benoit.pouffary@cnes.fr

ABSTRACT

The objective of the present note is to provide the basic concepts of numerical modelling of cavitation. After a brief description of the cavitation phenomena, the modelling concepts are discussed. A specific attention is given to the development of a barotropic model and its integration in a 3D unsteady CFD code. Influence of numerical and physical parameters is detailed on two two-dimensional configurations (hydrofoil and venturi). Examples of calculations on various geometries (inducers and impellers) are detailed to validate robustness of the computational methodology. Modifications of internal flows due to development of cavitation are discussed and an analysis of the mechanisms leading to the head drop is presented. Simulations of cavitation instabilities in blade cascades are presented and physical mechanisms are discussed.

NOMENCLATURE

c	Chord (m)
C_p	Pressure coefficient : $C_p = \frac{P - P_{ref}}{\frac{1}{2} \rho U_{ref}^2}$
C_l, C_d	Lift and drag coefficients per span unit $C_{l,d} = \frac{Force}{\frac{1}{2} \rho U_{ref}^2 c}$
NPSH	Cavitation parameter : $NPSH = \frac{P_{tot}^{entrée} - P_{vap}}{\rho g}$
P, P_s	Static pressure (Pa)
P_{tot}	Absolute total pressure (Pa)
P_{vap}, P_v	Vapour pressure (Pa)
Qn	Nominal flow rate (kg/s)
R	Radius (m)
St	Strouhal Number : $St = \frac{fl_{max}}{U_{ref}}$
Tu	Turbulence intensity : $Tu = \frac{\sqrt{\frac{2}{3} k}}{U_{ref}}$

Report Documentation Page				Form Approved OMB No. 0704-0188	
Public reporting burden for the collection of information is estimated to average 1 hour per response, including the time for reviewing instructions, searching existing data sources, gathering and maintaining the data needed, and completing and reviewing the collection of information. Send comments regarding this burden estimate or any other aspect of this collection of information, including suggestions for reducing this burden, to Washington Headquarters Services, Directorate for Information Operations and Reports, 1215 Jefferson Davis Highway, Suite 1204, Arlington VA 22202-4302. Respondents should be aware that notwithstanding any other provision of law, no person shall be subject to a penalty for failing to comply with a collection of information if it does not display a currently valid OMB control number.					
1. REPORT DATE 01 NOV 2006		2. REPORT TYPE N/A		3. DATES COVERED -	
4. TITLE AND SUBTITLE Numerical Modelling of Cavitation				5a. CONTRACT NUMBER	
				5b. GRANT NUMBER	
				5c. PROGRAM ELEMENT NUMBER	
6. AUTHOR(S)				5d. PROJECT NUMBER	
				5e. TASK NUMBER	
				5f. WORK UNIT NUMBER	
7. PERFORMING ORGANIZATION NAME(S) AND ADDRESS(ES) CNES Launcher Directorate Rond Point de l'Espace 91023 Evry Cedex FRANCE				8. PERFORMING ORGANIZATION REPORT NUMBER	
9. SPONSORING/MONITORING AGENCY NAME(S) AND ADDRESS(ES)				10. SPONSOR/MONITOR'S ACRONYM(S)	
				11. SPONSOR/MONITOR'S REPORT NUMBER(S)	
12. DISTRIBUTION/AVAILABILITY STATEMENT Approved for public release, distribution unlimited					
13. SUPPLEMENTARY NOTES See also ADM002051., The original document contains color images.					
14. ABSTRACT					
15. SUBJECT TERMS					
16. SECURITY CLASSIFICATION OF:			17. LIMITATION OF ABSTRACT UU	18. NUMBER OF PAGES 54	19a. NAME OF RESPONSIBLE PERSON
a. REPORT unclassified	b. ABSTRACT unclassified	c. THIS PAGE unclassified			

U_{ref}	Reference velocity (m/s)
V	Absolute velocity
y_{paroi}	distance to the wall (m)
u_τ	vitesse de frottement : $u_\tau = \sqrt{\frac{\tau_{paroi}}{\rho}}$
y^+	distance to the wall : $y^+ = \frac{\rho u_\tau y_{paroi}}{\mu}$
α	Void fraction
ε	Turbulent dissipation
γ	Surface tension (J/m ²)
μ	Viscosity
μ_t	Turbulent viscosity
ρ	Density (kg/m ³)
ρ_l, ρ_v	Liquid and vapour density (kg/m ³)
σ	Cavitation parameter: $\sigma = \frac{P_{ref} - P_{vap}}{\frac{1}{2} \rho U_{ref}^2}$
ω	Rotation speed (rad/s)
Ω	Cell volume (m ³)

1.0 INTRODUCTION

In the frame of the development of a rocket engine turbopump, cavitation is one of the most limiting hydraulic constraints. For this reason, CNES and Snecma have been working in collaboration with LEGI laboratory and Numeca in order to develop a CFD code being able to predict the cavitating flows developing in rocket engine turbopumps. For this presentation, cavitation will be considered assuming no thermal effects.

1.1 Cavitation

Cavitation relates to the liquids submitted to pressure lower than their saturating vapour pressure. The liquid phase is then metastable and operates a transition to vapour phase by formation of bubbles: this process is called cavitation. When cavitation appears in a flow, the physical properties are deeply modified in particular because of a brutal increase in compressibility of the gas/liquid mixture.

1.1.1 Vapour Structures

From a macroscopic point of view, cavitation can appear in various forms: by attached cavities, by bubbles or by localised vapour structures in shear layers. The internal structure of the cavities is complex and still badly known. However, experimental studies such as those performed by Stutz [20] have provided major informations on the characterisation of void fraction and velocity distributions. Thus, it has been observed that the cavitation sheets were very heterogeneous with void fraction values ranging from more than 80 % in the upstream part of a stable cavity to less than 10% in its downstream part. In the major part of the unsteady cavities the maximum values of void fraction do not exceed 20%.

1.1.2 Cavitation and Turbomachinery

The operation of an hydraulic machine generates localised depressions on the blades. When the decrease of static pressure is sufficient, it can lead to the appearance of cavitation that may deteriorate the performances of the machine. Consequently, cavitation has to be considered as an operational limit of the hydraulic machines:

- in term of maximum mass flow
- in term of height of installing. This last criterion is extremely important since it is mainly responsible for the realization costs in projects like: hydroelectric power plant, pressurisation devices installed on the water aduction networks, pumping stations...

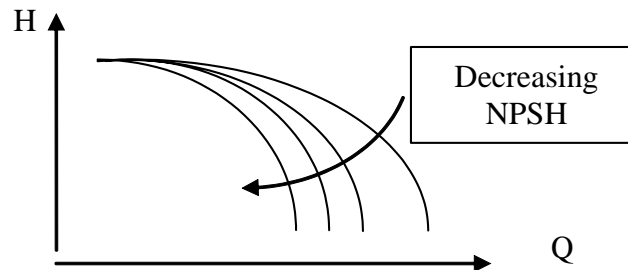


Figure 1.1: Modification of a Pump Characteristic Curve.

Finally, we focus on the problems that have motivated our work: cavitation developing in the rocket engine turbopumps.

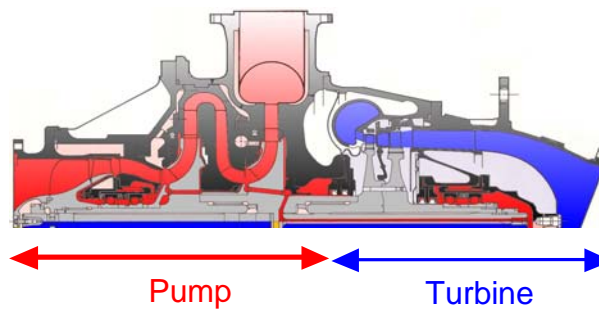


Figure 1.2: Vulcain LH2 Turbopump.

When a turbopump is running, cavitation may occur in the axial stage that is called inducer. Vapour cavities, when they are highly developed, cause a decrease of the pressure rise provided by the pump. The head drop occurs in a more or less brutal way according to the flow rate. In general, one observes that the lower the mass flow, the more brutal the head drop.

The second consequence of cavitation development in an inducer is the appearance of instabilities. Cavitation plays a role at system level (modification of hydraulic frequencies, damping) and at pump level. We focus on the instabilities that are intrinsic to the pump. Instabilities are associated with a rupture of the flow symmetry; thus, several configurations can be distinguished according to the cavity lengths on each blade:

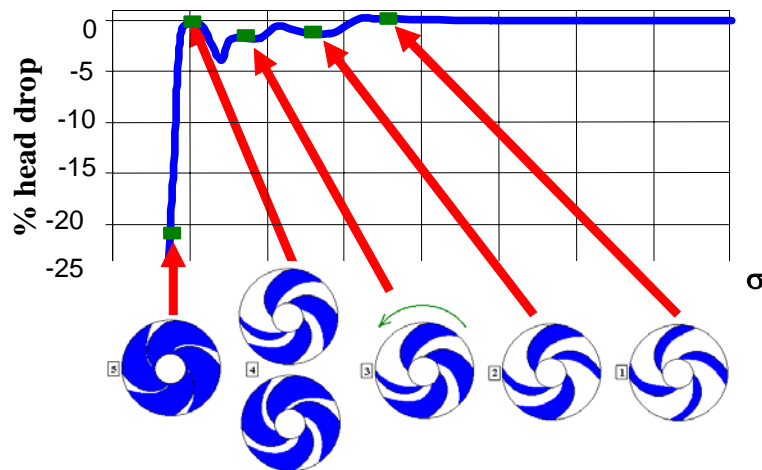


Figure 1.3: Cavitation Instabilities [4].

Two major instability configurations have been observed:

- Alternate cavitation is characterized by the coexistence of two small cavities intercalated between two longer cavities.
- Super synchronous cavitation is characterized by the presence of a small cavity surrounded by three longer cavities. As the small cavity turns in the relative frame in the direction of rotation of the machine one qualifies this configuration as super synchronous.

The consequences of these instabilities are dual: on the one hand, they induce pressure fluctuations upstream and downstream from the inducer and on the other hand, they generate radial loads that can be responsible of the crushing of the bearings.

1.2 Two-Phase Flow Fluid Mechanics

This paragraph is devoted to the presentation of the basics of two phase flow fluid dynamics.

1.2.1 One Fluid Conservation Equations

Fluid dynamics is governed by mass, momentum and energy conservation principles; these principle are classically expressed by the following local equations:

$$\frac{\partial \rho}{\partial t} + \nabla \cdot (\rho \mathbf{u}) = 0$$

$$\frac{\partial (\rho \mathbf{u})}{\partial t} + \nabla \cdot (\rho \mathbf{u} \otimes \mathbf{u}) = -\nabla p + \nabla \cdot \boldsymbol{\tau} + \rho \mathbf{f}_v$$

$$\frac{\partial (\rho h)}{\partial t} + \nabla \cdot (\rho h \mathbf{u}) = -\nabla \cdot \mathbf{q} + \frac{\partial p}{\partial t} + \mathbf{u} \cdot \nabla p + \phi$$

where ρ , \mathbf{U} , p , \mathbf{F}_v and H are respectively density, velocity, pressure, forces per unit of volume and enthalpy. These equations describe the temporal evolution of a single fluid flow. When two fluids are put together, an interface delimit the existence domain of each phase. We examine next how to model these patterns.

1.2.2 Discontinuities

Let us examine the effect of the introduction of discontinuities into the previous equations. We use as a convention $[x] = x_2 - x_1$ to describe the variation of a quantity x when crossing an interface. The conservation of an extensive scalar quantity per mass unit g is classically written as:

$$\frac{D}{Dt} \int_D \rho g dv = - \int_S \vec{\varphi} \cdot \vec{n} dS + \int_D \rho g_{vol} dv$$

This relation imposes when crossing an interface $\left[\left(\rho g \vec{V}_r + \vec{\varphi} \right) \cdot \vec{n} \right] = 0$ where \vec{V}_r is the relative speed to the interface.

- Mass conservation:

The mass conservation corresponds with the previous notations to $g=0$ and $\vec{\varphi}=\vec{0}$, which is written $\rho_1 \left(\vec{v}_1 - \vec{v}_i \right) \cdot \vec{n} - \rho_2 \left(\vec{v}_2 - \vec{v}_i \right) \cdot \vec{n} = 0$, that is to say: $\dot{m}_1 - \dot{m}_2 = 0$ where $\dot{m}_k = \rho_k \left(\vec{v}_k - \vec{v}_i \right) \cdot \vec{n}$ is the mass flow of the phase k through the interface. This relation illustrates the conservation of the total mass flow through the interface.

- Momentum conservation:

The quantity to be considered is $\vec{g} = \vec{V}$ and $\vec{\varphi} = -\vec{\sigma}$ where $\vec{\sigma}$ is the constraints tensor. Then, one can write $\left[\rho \vec{V}_r \cdot \vec{n} \vec{V} - \vec{\sigma} \cdot \vec{n} \right] = \gamma \kappa \vec{n} + \nabla_s \gamma$. The right-side term corresponds to the surface tension effects.

- Energy conservation:

The quantity to be considered is $g = e + \frac{1}{2} V^2$ and $\vec{\varphi} = \vec{q} - \vec{\sigma} \cdot \vec{V}$. Then, when neglecting the surface tension effects, one obtains: $\dot{m} \left([e] + \frac{1}{2} [V_r^2] \right) = - [\vec{q} \cdot \vec{n}] + [\vec{T} \cdot \vec{V}_r]$.

Thus, it appears that the equations used for traditional CFD for single phase flows can be easily extended to the diphasic problems. However, if this theoretical extension remains possible, it also appears that interfaces have to be characterised, which is a harsh numerical problem.

1.2.2 Averages

Just like for turbulence modelling, the description of all the diphasic structures leads quickly to multiplicity of the scales from temporal as well as from spatial point of view. If one is interested in the evolution of the macro-scales, it is natural to wonder about the relevance of an average approach. In theory, three approaches can be developed: the statistical average, the temporal average or the space average. Just like for turbulence, the statistical average is difficult to implement hence the recurring use of the assumption of ergodicity justifying the use of temporal or spatial average.

The average approaches require the introduction of phase indicators X_k that are defined in the following way:

$$X_k(\vec{x}, t) = \begin{cases} 1 & \text{if } \vec{x} \text{ belongs to phase } k \\ 0 & \text{elsewhere} \end{cases}$$

This phase indicator function allows to define the phase k existence domain \mathcal{D}_k like the set of points \vec{x} for which $X_k(\vec{x}, t) = 1$ at instant t . This \mathcal{D}_k quantity is used to define the volume fraction of phase k inside the whole domain: $\mathcal{D} = \sum_k \mathcal{D}_k$ and $\mathcal{R}_k = \frac{\mathcal{D}_k}{\mathcal{D}}$. To describe cavitating flows, the more usual parameter is void fraction α defined as the vapour volume fraction.

Two space averages are commonly used:

- The average on the whole domain: $\langle f \rangle = \frac{1}{\mathcal{D}} \int_{\mathcal{D}} f d\mathcal{D}$
- The average on the phase k existence domain: $\langle f \rangle = \frac{1}{\mathcal{D}_k} \int_{\mathcal{D}_k} f d\mathcal{D}$

From the temporal point of view, a space point \vec{x} is fixed and one defines the concept of presence time of the phase k T_k as the set of instants t when the phase k is located in \vec{x} .

Two time averages are commonly used:

- The average over the time interval T : $\bar{f} = \frac{1}{T} \int_T f dt$
- The average over the presence time of the phase k : $\bar{f} = \frac{1}{T_k} \int_{T_k} f dt$

Lastly, by analogy with the volume fraction associated to the spatial point of view, a temporal fraction can be defined as $\alpha_k = \frac{T_k}{T}$. Assuming ergodicity leads to identify the averages and the concepts of volume and temporal fraction.

To develop a numerical model with finite volume methods based on an averaged approach, it is necessary to apply the space average operator to the instantaneous local equations. This operation is quite detailed in many books on two phase flows ([6] for example). These calculations lead for each phase to the following averaged equations:

- Mass conservation:

$$\frac{\partial \mathcal{R}_k \rho_k}{\partial t} + \vec{\nabla} \cdot (\mathcal{R}_k \rho_k \vec{U}_k) = \Gamma_k$$

where Γ_k is the mass creation rate of the phase k .

- Momentum conservation for each phase:

$$\frac{\partial \mathcal{R}_k \rho_k \vec{U}_k}{\partial t} + \vec{\nabla} \cdot (\mathcal{R}_k \rho_k \vec{U}_k \vec{U}_k) = \rho_k \vec{F} + \nabla T_k$$

- Energy conservation for each phase:

$$\frac{\partial \mathcal{R}_k \rho_k E_k}{\partial t} + \nabla \left(\mathcal{R}_k \rho_k E_k \vec{U}_k \right) = \rho_k \vec{F} \cdot \vec{U}_k + \nabla T_k \cdot \vec{U}_k - \nabla q_k$$

where $E_k = \frac{1}{2} U_k^2 + e_k$, with E energy internal.

In each equation some source terms appear (mass transfer Γ_k , volume and surface forces F_K T_K , heat flux q_k) that have be modelled: they include in particular the interfacial effects averaged over the control volume.

2.0 PHYSICAL MODELS

The models that are developed to simulate cavitation phenomena can be gathered in two main classes: the direct models and the averaged models.

2.1 Direct Diphasic Models

We define as direct diphasic models, the models that intend to solve all the diphasic structures. Two approaches can be followed to establish the equations to be solved: Lagrange approach and Euler approach.

2.1.1 Lagrange Approach

The Lagrange approach consists in solving the movement equations of a particle on its trajectory in order to calculate the evolution of its position and speed. Considering a set of rigid particles for which heat and mass transfer can be neglected, the system to be solved is the following:

$$\begin{aligned} \frac{d \vec{x}_p}{dt} &= \vec{u}_p \\ m_p \frac{d \vec{u}_p}{dt} &= \sum \vec{F}_i \\ I_p \frac{d \vec{\omega}_p}{dt} &= \vec{T} \end{aligned}$$

where m_p is the mass of the particle, I_p its moment of inertia, \vec{F}_i the forces acting on the particle and \vec{T} the torque generated by a viscous fluid on a rotating particle.

Analytical solutions for the various forces and the torque are available only for small particle Reynolds numbers (Stokes configuration). The extension of these results to higher Reynolds numbers is in general based on empirical correlations.

The various models can be gathered in three classes according to the level of fluid/particle interactions [19]. The first level of simplification (one-way coupling) consists in considering that forces acting on a particle are only lift and drag; moreover, the effect of lift and drag is limited to a single particle (no action on fluid flow nor other particules). The second level of simplification (two-way coupling) consists in adding the interaction with the liquid taking into account mass, momentum and energy transfers. Lastly, the most complex models (four-way coupling) take into account the interactions between the particles. At

present time, it seems that the applications of this type of methods to cavitation modelling is mainly limited to the study of the cavitation nuclei. The justification of a level of approximation is done according to the dispersion of the two phase flow.

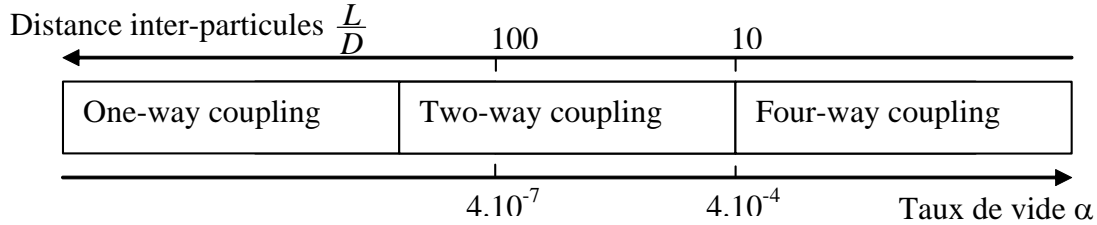


Figure 2.1: Evolution of the Distance Inter-Particles According to the Void Fraction.

2.1.2 Euler Approach

The Euler approach is based on the resolution of the Navier-Stokes equations combined with a reconstruction technique of the interfaces. For several decades, a major effort has been carried out on the basis of VOF (Volume Of Fluid) method. For the presentation of these methods, we will place ourselves in the case of a two-dimensional grid with of constant space steps ($H = \Delta x = \Delta y$). The “Volume Of Fluid” calling comes from the introduction of the fluid fraction $C_{i,j}$ defined by $C_{i,j}h^2 = \iint_{i,j} H(x,y)dx dy$ where

H is the characteristic function of the fluid (H is equal to 1 in the fluid and 0 elsewhere). Consequently, C takes values ranging between 0 and 1 when the mesh is cut by an interface, while it equals 0 or 1 elsewhere. The description of the vapour structures is then relying on the reconstruction and propagation of this interface. The two most famous techniques used to determine the interface position are SLIC (Simple Line Interface Calculation) and PLIC (Piecewise Linear Interface Construction) methods.

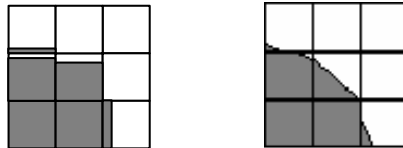


Figure 2.2: Interface Computed by SLIC and PLIC Method.

The difference between the two techniques lies in the fact that local interface in each cell is imposed or not to be aligned with a cell frontier.

2.2 Averaged Models

When the void fraction values become higher than 4.10^{-4} , the interactions between particles must be taken into account, which generates a lot of difficulties to use direct models. As the difficulties that have to be faced are similar to those induced by turbulence (multiplication of the space scales), we adopt the same kind of approach that has been developed for turbulence modelling. Just like for RANS turbulence models, we will distinguish several classes of modelling according to the number of equations used to model the diphasic structures. The common point of all these models is the use of the mixture conservation equations. The variables in the mixture are defined by averaging the variables of each phase:

- density: $\rho_m = \alpha\rho_v + (1-\alpha)\rho_l$
- momentum: $(\rho u)_m = \alpha(\rho u)_v + (1-\alpha)(\rho u)_l$

- energy: $(\rho E)_m = \alpha(\rho E)_v + (1 - \alpha)(\rho E)_l$

2.2.1 Models with n (n ≥ 2) Equations

Having n equations with n ≥ 2 means that the slip between the phases (different speeds for the liquid and the vapour) has to be taken into account. The additional equations with respect to the mixture conservation equations are conservation equations of liquid or vapour. The more equations you try to solve the more closing terms you have to model.

2.2.2 1 Equation Models

In these models, a no slip condition between the phases is assumed. The only additional equation that has to be solved is the mass conservation of liquid or vapour:

$$\begin{aligned}\frac{\partial \rho}{\partial t} + \nabla(\rho \vec{u}) &= 0 \quad \text{mass conservation of the mixture} \\ \frac{\partial \alpha \rho_v}{\partial t} + \nabla(\alpha \rho_v \vec{u}) &= \Gamma_v \quad \text{mass conservation of the vapour}\end{aligned}$$

The modelling effort then consists in determining a formulation of the source term Γ_v .

2.2.2.1 Use of the Rayleigh-Plesset Equation

The Rayleigh-Plesset equation describes the evolution of the radius of a spherical bubble located in an infinite incompressible fluid that is supposed to be at steady state.

$$\frac{p_B - p_\infty}{\rho_l} = R \frac{d^2 R}{dt^2} + \frac{3}{2} \left(\frac{dR}{dt} \right)^2 + 4 \frac{\nu_l}{R} \frac{dR}{dt} + \frac{2\gamma}{\rho_l R}$$

For practical modelling of cavitation in CFD codes, this equation is simplified by neglecting surface tension, viscosity and second order time dependence:

$$\frac{dR}{dt} = \text{sgn}(P_v - P) \sqrt{\frac{2}{3} \frac{|P_v - P|}{\rho_l}}$$

Assuming that the bubbles density n is uniform and constant, the evolution of the void fraction is straight forward as the vapour volume is $n \frac{4}{3} \pi R^3$. Concerning this approach, it has to be kept in mind that the Rayleigh-Plesset equation is not solved and that the reference to bubbles is artificial: the most basic expression of Rayleigh-Plesset equation is simply used to formulate a source term for vaporisation in the frame of a single fluid model.

2.2.2.2 Empirical Modelling of the Source Terms

To take into account the convection of void fraction, one can work directly on modelling vaporisation and condensation rate so that they can be included in vapour mass conservation equation:

$$\frac{\partial \alpha \rho_v}{\partial t} + \nabla(\alpha \rho_v \vec{U}) = -(\dot{m}^- + \dot{m}^+).$$

Following formulations proposed by Kunz allowed to get good numerical results:

- Vaporisation rate: $\dot{m}^- = \frac{C_{dest} \rho_l \alpha \min(0, p - p_v)}{\frac{1}{2} \rho_l U_\infty^2 t_\infty}$
- Condensation rate: $\dot{m}^+ = \frac{C_{prod} \rho_v \alpha^2 (1 - \alpha)}{t_\infty}$

C_{dest} and C_{prod} have to be tuned by comparison to experimental data.

2.2.3 0 Equation Models

For 0 equation models, only the mixture equations are solved. Consequently, a barotropic state law describing the behaviour of the mixture has to be proposed. The density evolution is generally described by a piecewise defined function:

$$\rho = \begin{cases} \rho_L & \text{if } p > p_v + \Delta p \\ \rho_v & \text{if } p < p_v - \Delta p \\ \rho(p) & \text{if } p_v - \Delta p < p < p_v + \Delta p \end{cases}$$

where Δp is half-width of the transition from vapour to liquid. Three functions are usually used to ensure the transition between the vapour and the liquid: integration of analytical formula of speed of sound, polynomial connection and sinusoidal connection.

- In a liquid / incondensable gas mixture, the speed of sound can be easily calculated from the speed of sound in each phase and the void fraction value. Indeed, for a stationary diphasic mixture without mass transfer:

$$\frac{1}{\rho_m c_m^2} = \frac{\alpha}{\rho_g c_g^2} + \frac{1 - \alpha}{\rho_l c_l^2}, \text{ and then}$$

$$\frac{1}{c_m^2} = \left[\alpha \rho_g + (1 - \alpha) \rho_l \right] \left[\frac{\alpha}{\rho_g c_g^2} + \frac{1 - \alpha}{\rho_l c_l^2} \right]$$

Assuming that the speed of sound doesn't depend on entropy, it comes $c_m^2 = \frac{dP}{d\rho}$. Lastly, the integration of this equation between $p_v + \Delta p$ and the local pressure provides the density value [7].

- Connection from liquid to vapour can be defined with a polynomial connection [17]:

$$p = \sum_{i=0}^5 A_i \rho^i$$

Coefficients A_i are chosen to ensure continuity with liquid and vapour phases; moreover, they are selected in order to obtain a sharp density gradient when cavitation appears.

- Last, connection from liquid to vapour can be defined with a sine function:

$$\rho = \frac{\rho_l + \rho_v}{2} + \frac{\rho_l - \rho_v}{2} \sin\left(\frac{P - P_v}{c_{\min}^2} \frac{2}{\rho_l - \rho_v}\right)$$

where c_{\min} corresponds to the minimal speed of sound in the mixture. This model has been developed at LEGI for CNES purposes since the early 90's [5]. All the results presented in the next paragraphs are obtained with this model.

Two independent parameters are characterising this law: ρ_v and c_{\min} . The vapour density should not be a parameter since its value is known. However, this value is so low ($0,0256 \text{ kg/m}^3$ for water) that it can generate many numerical problems: the strong non linearity of the law associated with a very low value ρ_v value requires a particularly strict numerical processing. Consequently, ρ_v becomes a parameter of the law whose influence must be estimated. Moreover, as ρ_v is not imposed at the vapour density value, it has to be considered as the minimum density value of the mixture. When comparing to experimental results, this hypothesis is well validated as maximum void fraction value is around 90 %; indeed, some water drops remain present inside the cavitation sheets. Concerning the c_{\min} value, the problem is definitely more complex since measurement of speed of sound in cavitating flows is not so easy. Consequently, this value has been tuned by comparison to experimental data; in our calculations, the value of c_{\min} is 2,25m/s.

3.0 PRESENTATION OF THE SOLVER

In this part, we give a description of Euranus that is the Fine/Turbo™ solver in which the cavitation models developed at LEGI have been integrated. Fine/Turbo™ is a complete CFD package (grid generator, solver and post-processing) developed by Numeca International.

3.1 Introduction

The spatial discretization is based on a finite volumes approach; numerical scheme can be either centred or decentered. The integration is based on an explicit time-marching method. During each iteration a four steps Runge-Kutta scheme is used.

We first discuss about the way (local or global) the pseudo time step is calculated. We will always speak about time step within the meaning of pseudo time with respect to the time-marching algorithm. The step in real time will be explicitly called physical time step. The choice of a local time step means that the time step value will be different in each cell for a single time step. Indeed, it is the CFL (Courant Friedrichs Lewy) number that is kept constant to guaranty the stability. Consequently, as the time step is given by $\frac{\Delta \tau}{\Omega} = \frac{CFL}{\rho_s}$ where Ω is the cell volume and ρ_s the spectral radius (the details on the calculation of the time

step will be given next), it appears that the time step value will depend on the cell as Ω and ρ_s are local variables. If one uses a global time step, then the minimum value of the local time steps will be used for each cell, inducing a lower convergence speed.

3.1.1 System of Equations

The fluid dynamics equations presented in previous paragraph can be easily written in a conservative vector form.

$$\frac{\partial}{\partial t} \int_{\Omega} \vec{U} d\Omega + \oint_{\partial\Omega} \vec{F} dS = \int_{\Omega} \vec{ST} d\Omega$$

where \vec{U} is the vector of the conservative variables $\vec{U} = \begin{pmatrix} \rho \\ \rho u \\ \rho v \\ \rho w \end{pmatrix}$ and \vec{ST} the source term.

3.1.2 Space Discretization and Calculation of Fluxes

The space discretization is based on storage of the variables at the centre of the cells. The calculation of fluxes is carried out by summing fluxes on each face of the cell. Convective fluxes are calculated as follows:

$$\left[\vec{F}(\vec{U}) \cdot \vec{n} \right]_{i+\frac{1}{2}} = \vec{F} \left(\frac{\vec{U}_i + \vec{U}_{i+1}}{2} \right) \cdot \vec{n} - d_{i+\frac{1}{2}}$$

$d_{i+\frac{1}{2}}$ is numerical dissipation that is necessary to stabilize the centred schemes. Its calculation utilizes differences of the conservative variables at 2nd and 4th order:

$$d_{i+\frac{1}{2}} = \varepsilon_{i+\frac{1}{2}}^{[2]} \Delta U_{i+\frac{1}{2}} + \varepsilon_{i+1}^{[4]} \left(\Delta U_{i+\frac{3}{2}} - \Delta U_{i+\frac{1}{2}} \right) - \varepsilon_i^{[4]} \left(\Delta U_{i+\frac{1}{2}} - \Delta U_{i-\frac{1}{2}} \right)$$

where Δ is the centred differential operator: $\Delta U_{i+\frac{1}{2}} = U_{i+1} - U_i$.

Coefficients $\varepsilon^{[2]}$ and $\varepsilon^{[4]}$ are respectively: $\varepsilon_{i+\frac{1}{2}}^{[2]} = \frac{1}{2} \nu_0^{[2]} \tilde{\lambda}_{i+\frac{1}{2}} \max(s_{i-1}, s_i, s_{i+1}, s_{i+2})$

$$\varepsilon_{i+\frac{1}{2}}^{[4]} = -\max \left(0, \frac{1}{2} \nu_0^{[4]} \tilde{\lambda}_{i+\frac{1}{2}} - \varepsilon_{i+\frac{1}{2}}^{[2]} \right) \text{ and } \varepsilon_i^{[4]} = \frac{1}{2} \left(\varepsilon_{i+\frac{1}{2}} + \varepsilon_{i-\frac{1}{2}} \right)$$

Default values of $\nu_0^{[2]}$ and $\nu_0^{[4]}$ are 1.0 and 0.1. The s_i coefficients are activators proportional to the

pressure gradients: $s_i = \left| \frac{p_{i+1} - 2p_i + p_{i-1}}{p_{i+1} + 2p_i + p_{i-1}} \right|$

Lastly, the variable $\tilde{\lambda}$ is equal to the spectral radius (maximum eigenvalue) of the convective fluxes matrix multiplied by the surface and corrected with a function introduced by Martinelli and Jameson (1988) to increase dissipation in the directions where the grid is stretched.

3.1.3 Temporal Integration and Dual Time Step

Dual time stepping consists in using for the resolution of the unsteady equations an additional pseudo-time derivative:

$$\iiint_V \frac{\partial U}{\partial \tau} dV + \frac{\partial}{\partial t} \iiint_V U dV + \iint_S \vec{F} \cdot \vec{dS} = \iiint_V S dV$$

Thus, each physical time step is regarded as a stationary problem whose solution is obtained via iterations in pseudo-time. When convergence is reached, the pseudo-time derivative is null and the traditional unsteady equation is verified. In the particular case of a steady calculation, the equation to be solved does not contain the temporal terms:

$$\iiint_V \frac{\partial U}{\partial \tau} dV + \iint_S \vec{F} \cdot \vec{dS} = \iiint_V S dV$$

Thus, it is noted that the discretized problem (steady or unsteady) is always locally expressed as:

$$\frac{\partial U}{\partial \tau} \Omega + R(U) = 0$$

By definition, R is called residual. Temporal integration (in fact, pseudo temporal) is carried out for each iteration by an explicit 4 steps Runge-Kutta process.

3.1.4 Preconditioning

For low Mach numbers the time marching algorithms are very slow. Indeed, convective eigenvalues U and acoustic eigenvalues $U \pm C$ become very different when the Mach number tends to 0 (low compressibility). One of the solutions to this problem is preconditioning: it consists in modifying the temporal derivative in the Navier-Stokes equations to obtain eigenvalues centred around U . As this term is not physical (it is cancelled at convergence), the solution is not modified. On the other hand, a very significant increase in convergence speed can be obtained. In the case of Euranus, the preconditioning was mainly developed by Hakimi [8].

$$\iiint_V \Gamma^{-1} \frac{\partial Q}{\partial \tau} dV + \frac{\partial}{\partial t} \iiint_V U dV + \iint_S \vec{F} \cdot \vec{dS} = \iiint_V S T dV$$

The resolution of a stationary problem is carried out by removing the temporal derivative. The Q vector corresponds to a new set of non conservative variables and Γ^{-1} is the preconditioning matrix

$$Q = \begin{pmatrix} p_g \\ u \\ v \\ w \end{pmatrix} \text{ and } \Gamma^{-1} = \begin{pmatrix} \frac{1}{\beta^2} & 0 & 0 & 0 \\ \frac{(1+\alpha)u}{\beta^2} & \rho & 0 & 0 \\ \frac{(1+\alpha)v}{\beta^2} & 0 & \rho & 0 \\ \frac{(1+\alpha)w}{\beta^2} & 0 & 0 & \rho \end{pmatrix}$$

$p_g = p - p_{ref}$ is a gauge pressure that limits the rounding errors.

Due to this modification of the equations, eigenvalues become:

$$\vec{V} \cdot \vec{n} \text{ and } \frac{1}{2} \left[\vec{V} \cdot \vec{n} (1 - \alpha) \pm \sqrt{(\vec{V} \cdot \vec{n} (1 - \alpha))^2 + 4 \vec{n}^2 \beta^2} \right]$$

Two parameters are used in this formulation of preconditioning: α that is in general equal to -1 and β that depends on a reference velocity ($\beta^2 = \beta_0 \cdot U_{ref}^2$).

3.2 Presentation of the Cavitation Module

In this part, we explain how the simulation of cavitation is integrated in the solver.

3.2.1 Density Calculation

On the one hand, the use of preconditioning imposes to calculate the pressure from the mass conservation equation: $p^{n+1} = p^n - RES * \Delta \tau * \beta^2$

In addition, the choice of a barotropic state law allows to deduce directly the density value from the pressure value: $\rho^{n+1} = \frac{\rho_l + \rho_v}{2} + \frac{\rho_l - \rho_v}{2} \sin\left(\frac{P^{n+1} - P_v}{c_{\min}^2} \frac{2}{\rho_l - \rho_v}\right)$

In order to smooth the density fluctuations, two procedures are used: relaxation and dissipation.

3.2.1.1 Relaxation

When a value of density is calculated by application of the barotropic state law, a relaxation is applied:

$$\rho^{n+1} = \rho^n + \alpha(\rho^{n+1} - \rho^n)$$

In order to respect the state law, the pressure is then calculated by inverting the state law:

$$p^{n+1} = p_v + \frac{\rho_l - \rho_v}{2} c_{\min}^2 \arcsin\left(\frac{\rho^{n+1} - \frac{\rho_l + \rho_v}{2}}{\frac{\rho_l - \rho_v}{2}}\right)$$

Moreover, an additional pressure relaxation has been added to control the phenomena of vaporization (respectively of condensation) starting from the pure liquid (respectively from the pure vapour).

3.2.1.2 Dissipation

The second order dissipation is activated in the zones of strong pressure gradients. However, cavitation is a phenomenon which is characterized by strong density gradients. Consequently, we advise to modify the calculation of second-order dissipation by taking into account density gradients

$$\varepsilon_{i+\frac{1}{2}}^{[2]} = \frac{1}{2} \tilde{\lambda}_{i+\frac{1}{2}} \max(\varepsilon_p, \varepsilon_\rho)$$

$$\text{where } \varepsilon_p = v_0^{[2]} \max(s_{i-1}^p, s_i^p, s_{i+1}^p, s_{i+2}^p) \text{ and } \varepsilon_\rho = RMUCAV \max(s_{i-1}^\rho, s_i^\rho, s_{i+1}^\rho, s_{i+2}^\rho)$$

Default value of RMUCAV is 1.0. The s_i^p coefficients are defined by:

$$s_i^p = \left| \frac{\rho_{i+1} - 2\rho_i + \rho_{i-1}}{\rho_{i+1} + 2\rho_i + \rho_{i-1}} \right|$$

3.2.2 Modifications of Resolution Process

The transition from an incompressible flow to an highly compressible flow generates strong modifications in the dynamic behaviour of the numerical scheme.

3.2.2.1 Eigenvalues

When one considers the flow of a compressible fluid, the eigenvalues of the system are modified; that is due to the dependence of pressure to density (explicit dependence on speed of sound). Thus, in the two phase areas one obtains the new eigenvalues:

$$\vec{V} \cdot \vec{n} \text{ and } \frac{1}{2} \left[\vec{V} \cdot \vec{n} \left(1 - \alpha + \frac{\beta^2}{c^2} \right) \pm \sqrt{\left(\vec{V} \cdot \vec{n} \left(1 - \alpha + \frac{\beta^2}{c^2} \right) \right)^2 + 4 \left(\frac{\vec{V} \cdot \vec{n}}{c^2} \right)^2} \right]$$

The modification of the calculation of the eigenvalues changes the local time step and the second-order dissipation which are respectively inversely proportional and proportional to the spectral radius.

3.2.2.2 Speed of Sound

The speed of sound appears explicitly in the expression of the spectral radius in the two phase zones; it is thus necessary to calculate it. Assuming that the speed of sound is independent from entropy it comes

$$c = \sqrt{\frac{dp}{d\rho}} \text{ and using the state law : } c = \frac{c_{\min}}{\sqrt{\cos\left(\frac{P - P_v}{c_{\min}^2} \frac{2}{\rho_l - \rho_v}\right)}}$$

3.2.2.3 Turbulence Model

The calculation of turbulent viscosity in the two phase zones can be carried out in two different ways. Either one uses the standard formulas, or the correction proposed by Reboud [18]:

$$\mu_t = \mu_t^s \frac{\rho_v + (1 - \alpha)^n (\rho_l - \rho_v)}{\rho} \text{ where } \mu_t^s \text{ is standard turbulent viscosity.}$$

4.0 UNSTEADY TWO DIMENSIONAL TEST CASES

From now on, we will focus on numerical results obtained with the barotropic model of cavitation that has been presented. We first examine unsteady results obtained in a venturi.

4.1 Computation Methodology

This paragraph is devoted to the presentation of the computation methodology to perform numerical simulations of unsteady cavitating flows. First, we focus on boundary conditions and on the way the cavitation is controlled. Then, we evoke the concept of convergence when performing unsteady calculations.

4.1.1 Boundary Conditions

For incompressible flows, boundary conditions are usually an imposed velocity at inlet and an imposed static pressure at outlet. With regard to the boundary conditions fixed on the solid walls, velocity is set to 0 (adherence at the wall). Depending on the turbulence model that is used (high Reynolds or low Reynolds), different grids have to be built. Thus, a high Reynolds model using a wall function allows to work with grids for which the first cell near a wall is associated with y^+ values ranging between 20 and 50 while a low Reynolds model requires values ranging between 1 and 10.

4.1.2 Cavitation Numbers

The development of cavitation is controlled by the non dimensional number: $\sigma = \frac{P_{ref} - P_{vap}}{\frac{1}{2} \rho U_{ref}^2}$. The

vapour pressure is a characteristic of the fluid and cavitation appears when the static pressure P_{ref}

decreases. For our calculations, we use the fact that the absolute value of static pressure does not play any role. Consequently, only the pressure gradients are effective so we can fix a constant reference pressure while varying the vapour pressure. Practically static pressure is imposed at outlet and the pseudo vapour-pressure is modified during an imposed number of physical time steps.

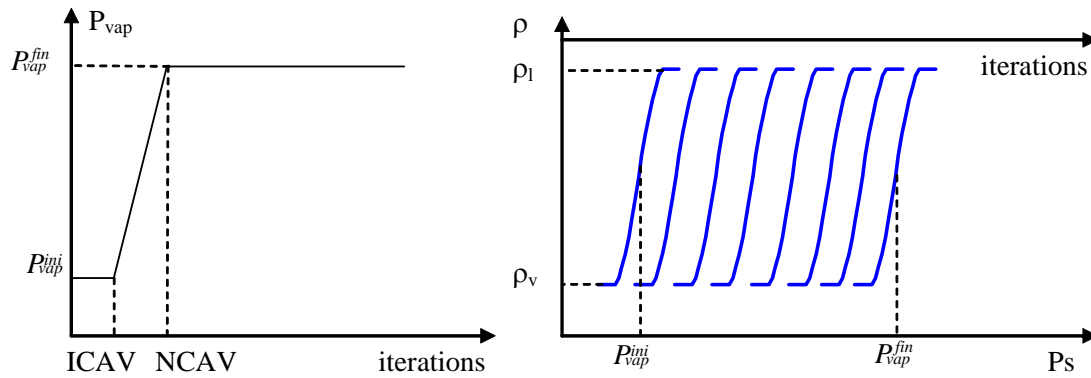


Figure 4.1: Evolution of the Vapour Pressure during the Calculation Transient.

With regard to the value of P_{vap} that is imposed for the first cavitating iteration, a margin is taken from the appearance of vapour. Thus, if ΔP is half-width of the barotropic law, the first value of vapour pressure is equal to $P_{mini} - 2 \Delta P$, where P_{mini} is the minimum value of static pressure in the flow. Thus, one avoids a brutal appearance of vapour that could lead to numerical instability. This procedure highlights the importance of using a very well converged non cavitating calculation as an initial condition in order to avoid pressure oscillations that would result instantaneously in the brutal appearance of vapour. Moreover, the non cavitating result is also used as a reference to quantify the modifications induced by cavitation.

4.1.3 Convergence for Unsteady Calculations

There is no clear rule that ensures a strict convergence of an unsteady calculation. nevertheless, several elements must be checked in order to avoid coarse errors:

- At mesh level, specific refinements must be carried out in order to be able to describe the unsteady structures of the flow. Consequently, a simple refinement of boundary layers is not sufficient.
- With regard to the physical time step value, it must be a fraction of the period of the studied phenomenon. In practice, we used time steps equal to 1/100 of the period estimated for the phenomenon to simulate.
- Today, two major criteria are used: number of pseudo time steps in each physical time step and residuals decrease. We will show next that these two methods are not sufficient to ensure a good convergence of unsteady calculations.

4.2 Venturi Computations

A deep analysis of the structure of the cavitation sheets developing in venturi channels was performed by Stutz [20]. This work has provided a great data base for the validation of our numerical work.

4.2.1 Numerical Study

In this paragraph, we present the characteristics of the geometry and the major numerical parameters.

4.2.1.1 Global Presentation

We first present the main characteristics of the geometry:

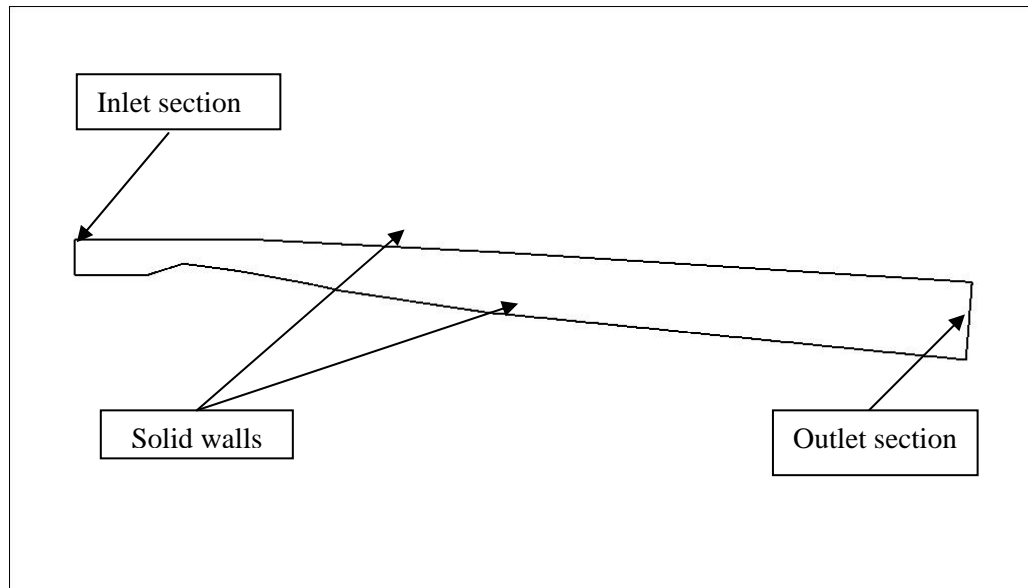


Figure 4.2: Geometry of the Venturi.

We performed a mesh convergence study on the three following meshes:

Table 4.1: Sizes of the Grids

Grid	number of nodes
1	81*801
2	60*150
3	60*265

A refinement of the mesh is performed in the boundary layers and in the throat section.

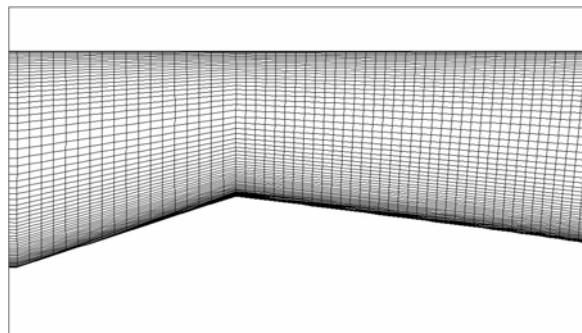


Figure 4.3: Local Mesh of the Throat.

4.2.1.2 Influence of the Numerical Parameters

The study of the influence of numerical parameters was focused on the determination of the necessary conditions allowing the simulation of vapour shedding downstream from a cavitation sheet. First of all, we present a typical residual evolution for an unsteady calculation.

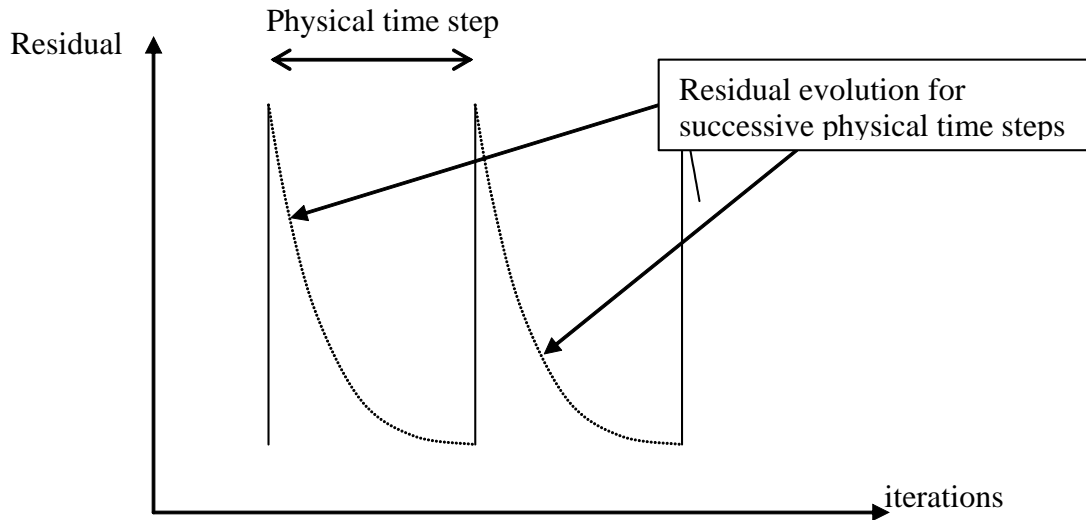


Figure 4.4: Convergence Curve for Unsteady Calculation.

A discontinuity is observed at the beginning of each time step when residuals are initialised; convergence will be reached if the number of internal iterations (pseudo time steps) is sufficient to get stabilisation of the residual at his minimum value.

Influence of the following parameters have been analysed:

- Transient duration:

For a number of time steps higher than 500 in the σ transient, the calculation led to steady cavitation at convergence. We were able to exhibit an unsteady behaviour of the cavitation sheet when imposing a transient of 100 time steps.

- Dissipation level:

Influence of 2nd order dissipation has been deeply analysed. It was found that a too high value of numerical dissipation leads to stabilisation of the computation.

- Convergence:

Convergence was validated by checking the residual stabilisation in each time step and by comparing the results obtained for 100 and 200 internal time steps. As no main modifications were observed, it could be concluded that the value of 100 was sufficient.

4.2.1.3 Influence of the Boundary Conditions

The main difficulty induced by the change of the boundary conditions lies in the comparison of the σ values. Indeed, when the static pressure is imposed at outlet, a $\sigma_{\text{downstream}}$ value based on this quantity is fixed. When the mass flow is imposed at outlet, this value of $\sigma_{\text{downstream}}$ is no longer fixed. In order to evaluate the importance of this change, we carried out a calculation by imposing total pressure at inlet and

mass flow at outlet. Then, the σ_{upstream} value based on inlet total pressure is kept constant in the calculation. This inlet total pressure value was imposed in order to get a σ_{upstream} value equal to the mean value of the computation performed with static pressure imposed at outlet. The result of the first computation was a large unsteady cavitation sheet whereas the result of the second computation was a little steady cavitation sheet. This result is very important because it shows that for an unsteady cavitating flow, the comparison with experimental results is highly dependant on the way you impose the σ value.

4.2.1.4 Influence of the Turbulence Models

We present now the influence of the turbulence model on cavitating unsteady calculations. Computations have been performed with Baldwin-Lomax, Spallart-Almaras, Chien k- ϵ , Launder-Sharma k- ϵ , Yang-Shih k- ϵ and wall functions k- ϵ models. Little discrepancies in the losses prediction led to high discrepancy when using the absolute pressure values to calculate σ values. The maximum variation has been observed between wall functions k- ϵ and Chien k- ϵ models. The uncertainty in static pressure values led to an uncertainty on σ_{upstream} value equal to 0,16, which is huge when comparing to observed dependence of cavity length to σ_{upstream} in the experiments

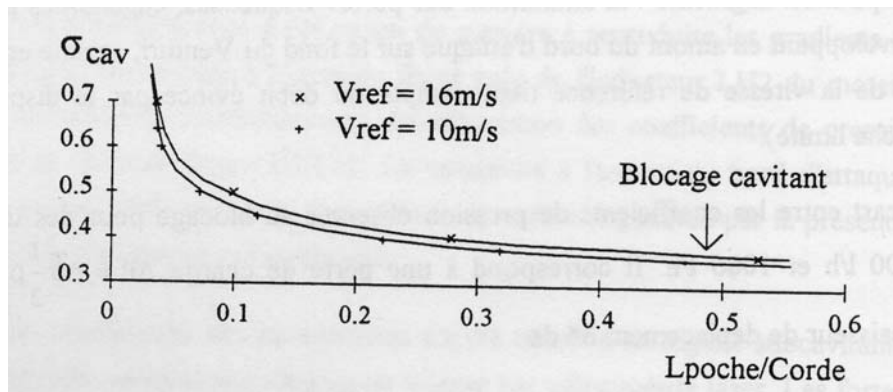
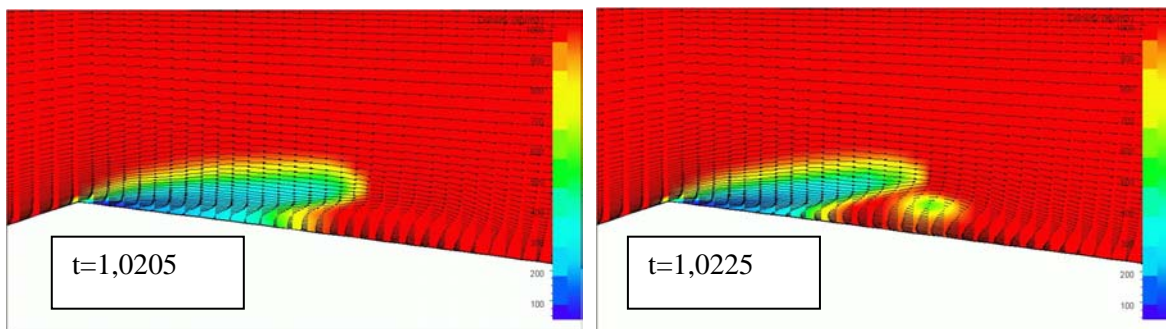


Figure 4.5: Cavity Length vs. σ in a Venture [20].

This results highlights again the difficulties inherent to the rigorous experimental validation of cavitating computations.

4.2.2 Analysis of the Flow

We present in this section a brief analysis of the cavitating flow that was computed in the venturi. We focus on the throat area where the cavitation sheet appears. The study is based on the evolution of density and velocity fields.



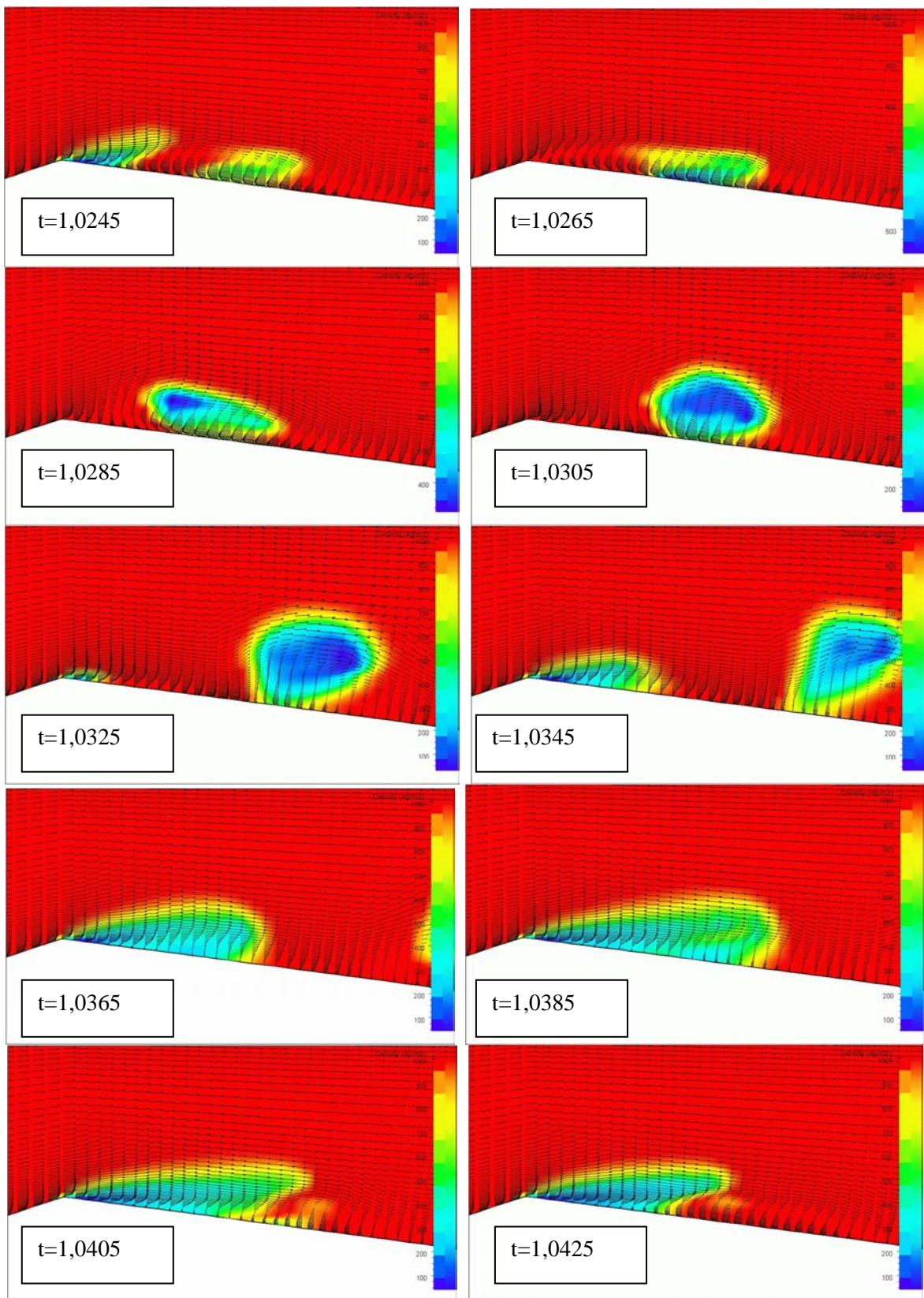


Figure 4.6: Cycle of Vapour Shedding.

Thus, the following mechanisms appear to be significant in the vapour shedding phenomenon:

- A first phase is associated to the decrease of the cavity length. This phase is characterized by the presence of a back flow at the closure area of the cavity. The inverse flow is localised near the lower wall: this phenomenon was observed in experiments [1]. It is from now on admitted that it plays a driving role for the generation of the vapour shedding. This first phase ends with the reinforcement of the back flow and the disappearance of the cavity.
- A second phase is characterized first by the brutal reattachment of the flow. Indeed, the disappearance of the cavity weakens the reverse pressure gradient that was creating the backflow. The vapour structure is then convected in a vortex ($t=1,0305$ s).
- The last phase is characterized by the appearance and the growth of a new cavitation sheet near the throat. The cavity grows until the development of a backflow in its closure area.

4.2.3 Convergence Analysis

This last part dedicated to the numerical simulation of cavitating flows in a venturi is focused on a simple convergence check that has shown that convergence is not so easy to reach.

The main numerical difficulties when performing cavitating computations with a preconditioned coupled solver are due to the mass conservation equation. Consequently, it is interesting to verify at each time step that mass conservation is well respected with respect to global considerations. As an example, we have analysed the space evolution of mass flow in the venturi channel for various time steps of an unsteady cavitating computation that seemed to be converged (decrease and stabilisation of the residuals for each time step).

In areas where the fluid has been a pure liquid since more than two physical time steps, the mass flow value should be constant (incompressibility consequence).

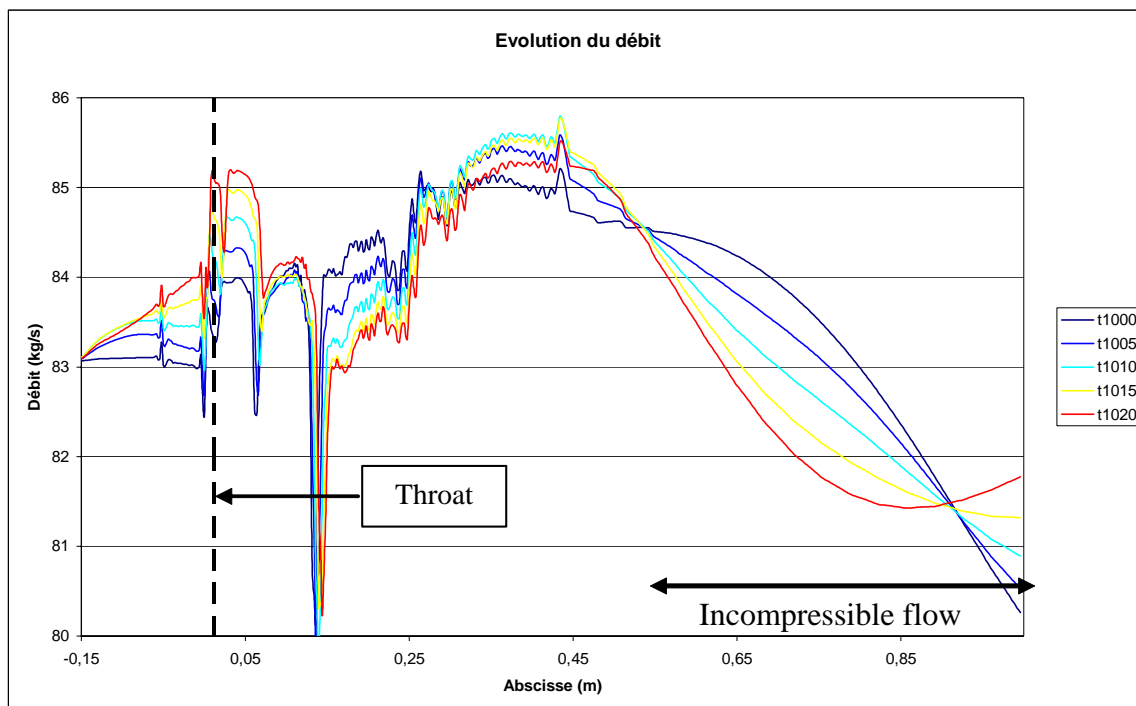


Figure 4.7: Space Evolution of Mass Flow for Successive Time Steps.

Each curve is corresponding to a specific instant. The vapour is localised in the zones where very sharp variations are observed. Thus, it appears that the mass flow is not constant even in areas where the liquid is definitely incompressible. The origin of the problem was clearly identified as a consequence of a too low number of internal iterations in each time step.

4.3 HYDROFOIL

To finish this chapter concerning the numerical simulation of unsteady cavitating flows, we present a work that was completed within the framework of a discussion on cavitation modelling for the 5th international symposium of cavitation CAV2003: for this occasion, a numerical test-case was defined in order to compare the results obtained with various models.

4.3.1 Presentation

The test-case is an hydrofoil that is placed in a channel (confined flow) and that is defined by the following analytical relation:

$$\left(\frac{y}{c}\right) = a_0 \sqrt{\frac{x}{c}} + a_1 \frac{x}{c} + a_2 \left(\frac{x}{c}\right)^2 + a_3 \left(\frac{x}{c}\right)^3 + a_4 \left(\frac{x}{c}\right)^4$$

where the constant a_0 to a_4 are respectively:

$$\begin{aligned} a_0 &= 0.11858 \\ a_1 &= -0.02972 \\ a_2 &= 0.00593 \\ a_3 &= -0.07272 \\ a_4 &= -0.02207 \end{aligned}$$

The cord is 10 cm ; concerning the channel, length is 1 m and width is 40 cm. Lastly, it has to be noted that the incidence angle is 7°. With regard to the boundary conditions, a uniform axial speed of 6 m/s as well as a turbulence intensity of 0,1% are imposed at inlet while a uniform static pressure of 10 bars is imposed at outlet.

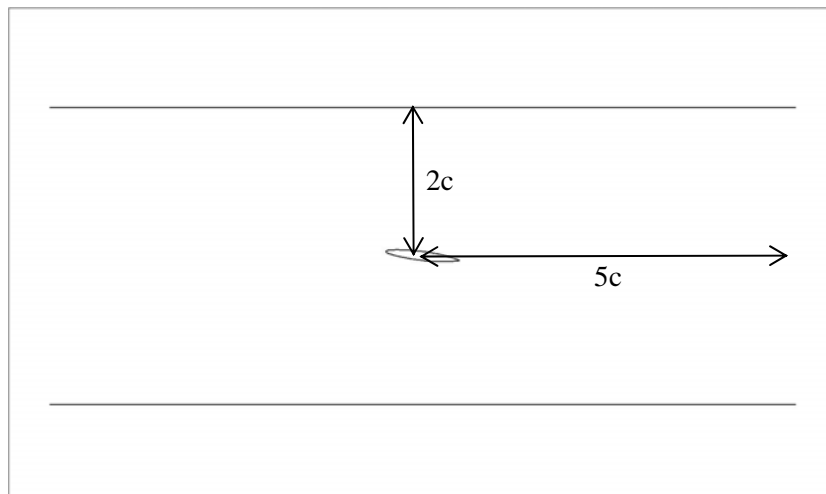


Figure 4.8: Geometry of the Hydrofoil.

The C-mesh used for the calculations is composed of 45000 cells (80*571).

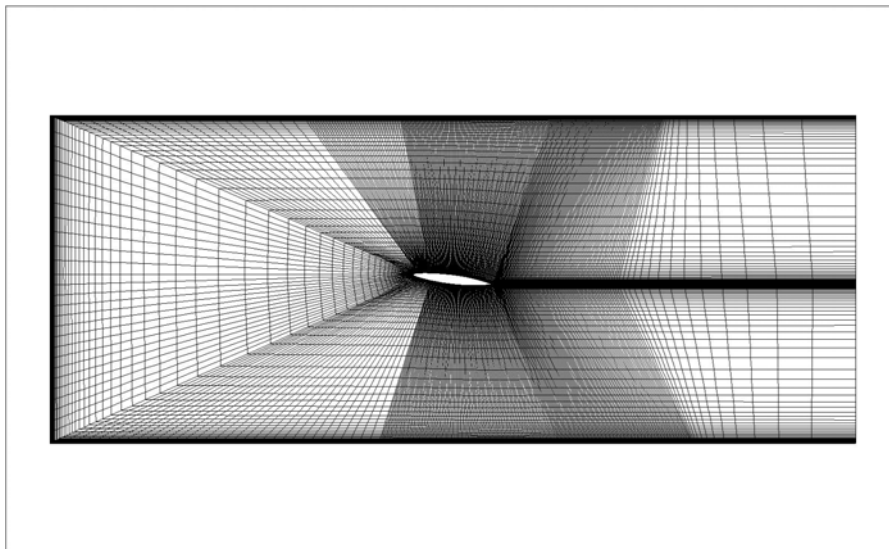


Figure 4.9: C-mesh.

The first cell size near a solid wall is around $50\text{ }\mu\text{m}$ to allow y^+ values on the foil between 4 and 8. Computations are performed with a standard $k-\varepsilon$ model with wall functions. The non cavitating simulations have predicted a lift coefficient of 0,56 and a drag coefficient of 0,03.

4.3.2 Analysis of Cavitating Flows for $\sigma = 0,8$

We first performed steady cavitating calculations for $\sigma = 0,8$. Assuming a steady hypothesis, the cavitation sheet obtained at convergence was stable. The development of this cavity induced a decrease in lift coefficient from 0,056 to 0,046 and an increase in drag coefficient from 0,03 to 0,05. As the cavity length was close to half the chord, unsteady calculations were next performed. These simulations exhibited a quasi-periodical behaviour of the flow that is illustrated by the lift coefficient evolution.

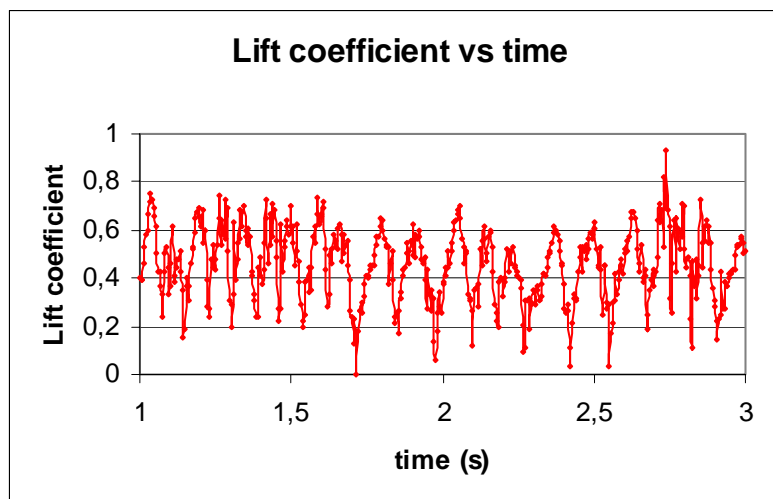


Figure 4.10: Temporal Evolution of the Lift Coefficient.

We next present the evolution of density field during a cycle.

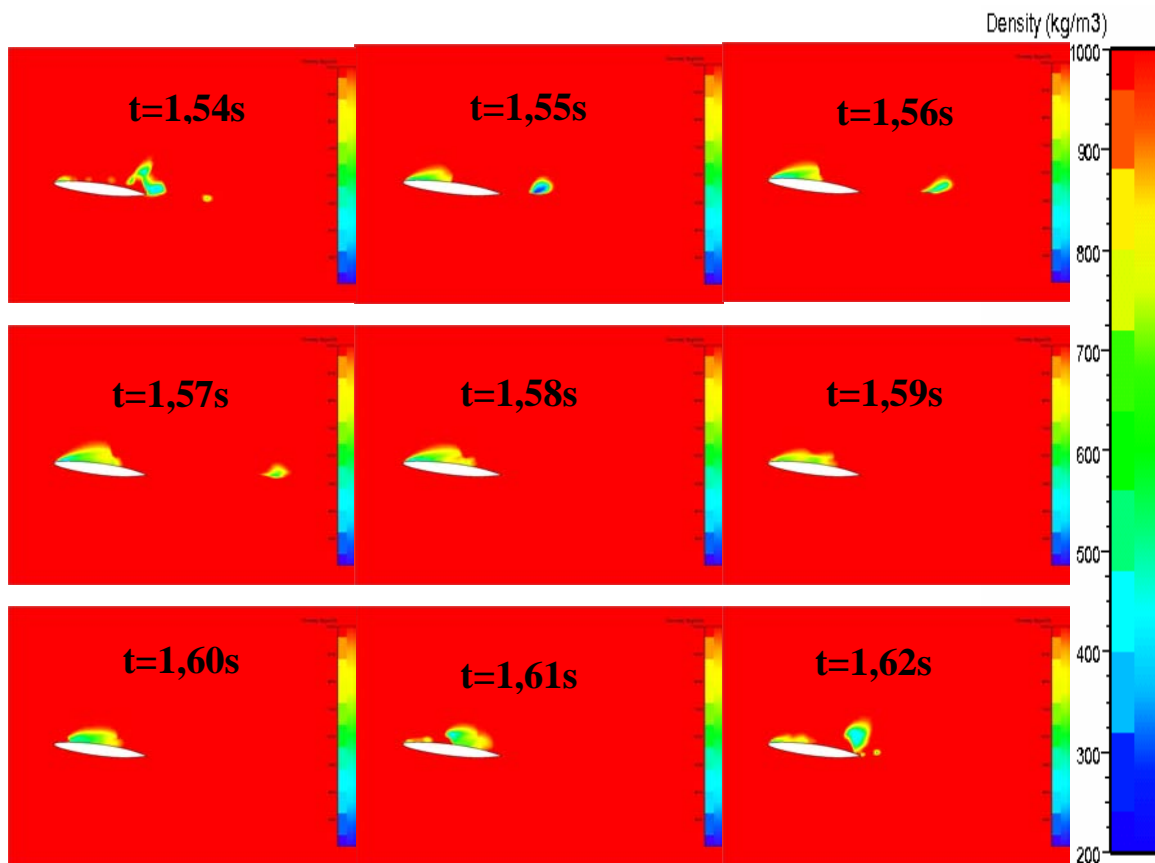


Figure 4.11: Time Evolution of Density Field.

A typical cycle can be divided in two phases: initially, the cavity grows while the cloud resulting from the previous shedding is convected downstream. This first phase is ended by the implosion of the vapour structures, which initiates the second phase characterized by a reduction in cavity length. Strouhal number of this periodic behaviour is 0,9.

Lift coefficient variations can be explained by comparing the evolution of load profiles and velocity field near the trailing edge to visualise the deviation generated by the foil.

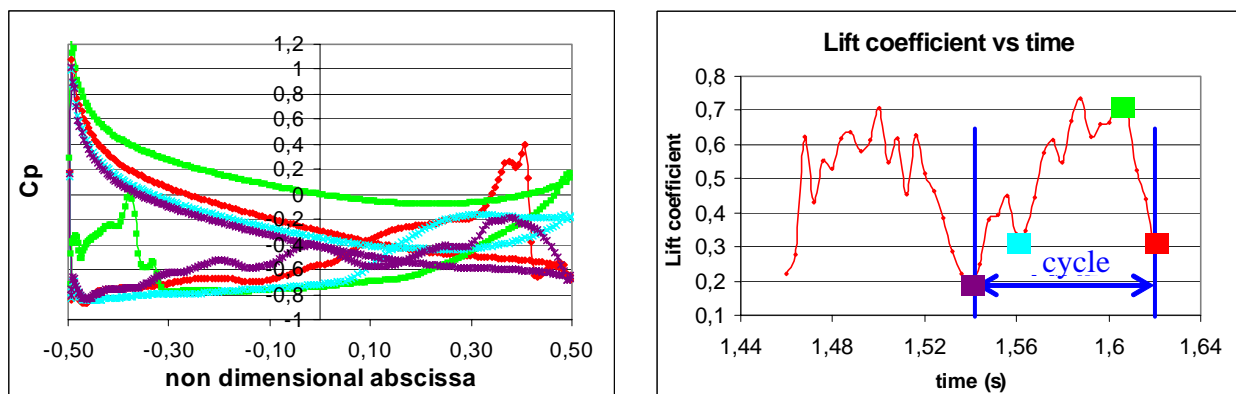


Figure 4.12: Load Profiles for Various Instants in a Lift Cycle.

It appears that the minimum of lift coefficient is reached (red and violet curves) when a load inversion occurs on second half of the chord. These instants correspond to $t=1,54s$ and $t=1,62s$ of figure 4.11. It can then be concluded that the worst cavitating configuration is not obtained for the longest cavity but when the vapour cloud reaches the trailing edge.

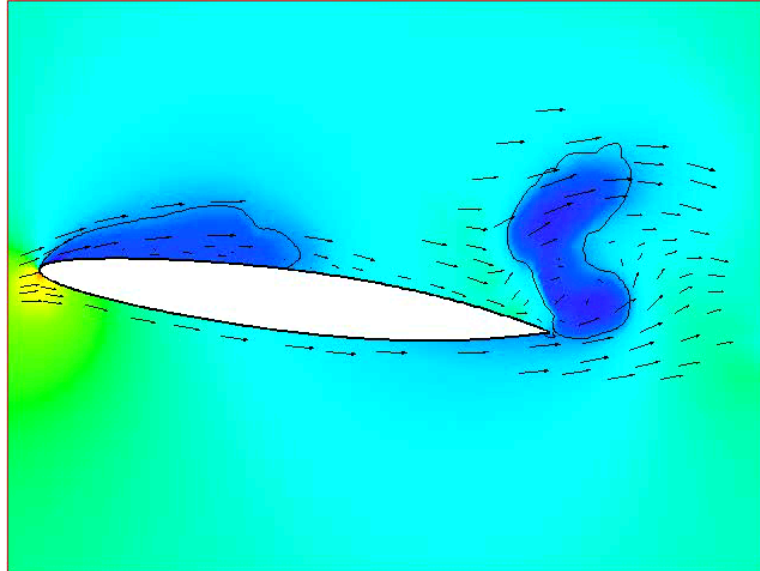


Figure 4.13: Velocity Field at Trailing Edge.

Black lines are the frontiers of two phase areas. This unsteady cavitating configuration led to a mean lift coefficient of 0,46 and a mean drag coefficient of 0,078. Consequently, it appears that the lift computed in the steady calculation is a good approximation of the mean value obtained in the unsteady one. Concerning the drag prediction, the conclusion is different as the mean drag value is 56% higher in the unsteady computation than the value obtained in the steady calculation.

5.0 NUMERICAL METHODOLOGY FOR TURBOMACHINERY

In this chapter, we focus on numerical specificities of the cavitating simulations in turbomachinery.

5.1 Presentation

Two main topics are discussed in this first part. First, the limits of the classical convergence criteria are discussed. Then, the influence of the computational methodology is examined.

5.1.1 Discussion on Convergence

From a theoretical point of view, convergence is well defined in the following way: “the discrete approximation is convergent if the unique discrete solution tends towards the exact solution when decreasing the time step Δt and the space step Δx towards 0.” In practice, it is impossible to verify these conditions when numerical schemes become complex (nominal case for CFD computations). Consequently, to characterise the convergence level of a calculation, some practical criteria have been defined that are based on the evolution of the residuals. Indeed, these variables represent exactly the error that is made in the conservation equations. The more common criterion is related to the decrease of the residuals. Usually if the residuals decrease of 4 orders of magnitude then calculation may be considered as converged. This evaluation is carried out by defining a global residual from the local residuals:

$$RES_{RMS} = \log \left(moy_{RMS} \left(\frac{RES(\Omega)}{\Omega} \right) \right)$$

The operator moy_{RMS} corresponds to RMS average and each residual RES is normalised with its initial value. Consequently, one will consider that the residuals have decreased of 4 decades when $RES_{RMS} = -4$. We think that this criterion requires a careful application for two reasons:

- On the one hand, the criterion is depending on the initial conditions: a badly initialized calculation will have a great decrease of the residuals without ensuring a good convergence.
- On the other hand, the criterion does not take into account the dynamic evolution of the residuals. Thus, this criterion does not consider as converged a calculation even if the solution doesn't evolve any more.

5.1.2 Methodology Impact on Head Drop Results

We present in this paragraph two major aspects of computational methodology for the simulation of cavitating flows:

- The choice of a procedure: step by step or continuous.
- The choice of a formulation of the equations: steady or unsteady.

In the past, head drop simulations were performed by decreasing continuously the cavitation number and by using unsteady formulation of the equations. We advise not to use this kind of computations but to perform multiple steady computations. The main objective is to master the convergence level by using robust criteria. To confirm this statement, we examine some of the consequences of an unsteady continuous procedure:

- The main reason explaining the use of unsteady formulation is a lack of stability. Indeed, the temporal derivative acts as a compensation term with respect to the brutal variations of pressure and density.
- A continuous variation of vapour pressure generates an anticipated prediction of head drop. As a proof element, we present the typical evolution of pressure rise for a steady cavitating computation of a rocket engine inducer (inducer 2 presented in §7).

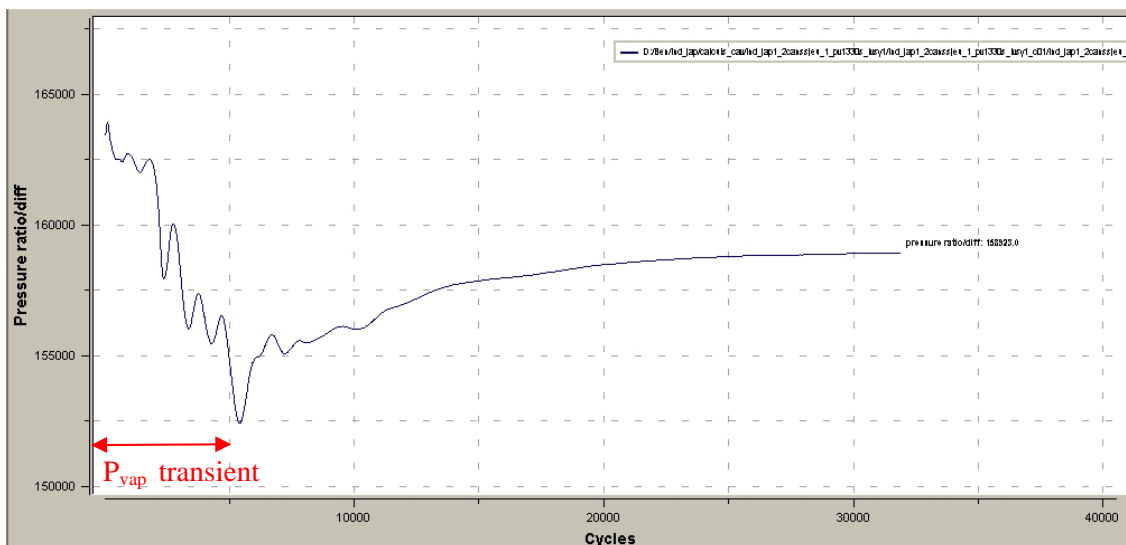


Figure 5.1: Evolution of Total Pressure Rise in the Course of Calculation.

Thus, it appears clearly that pressure rise decreases first when cavitation is developing (the transient on the vapour pressure is performed during the first 5000 iterations). When the decrease in vapour pressure is stopped, a pressure rise increase is observed, which proves that convergence was far from being reached at each time step.

5.2 Problems

Simulation of cavitating flows in turbomachinery generates specific problems with respect to numerical stability. The major problem is the transition from pure liquid to pure vapour of a cell in an single time step that can provoke brutal divergences. We next present how that occurs:

- We first mention that density is calculated from the pressure ; then, an abrupt variation of density is caused by a pressure step. As the pressure is determined by mass conservation equation, one deduces that the dynamic behaviour of this equation is responsible for the divergence.
- The mass conservation equation manages the evolution of the pressure by the following process: $p^{n+1} = p^n - RES * \Delta \tau * \beta^2$. RES corresponds to mass flow balance in the cell and $\Delta \tau$ is the pseudo time step. Then, this equation converts instantaneously an error in mass conservation into a pressure variation.
- Lastly, instability is due to sharp variations of density, which means that the problem can be identified as local with respect to the pressure field. Indeed, because of the stiffness of the state law, the transition from pure liquid to pure vapour can be caused by a variation of static pressure of about 0,1 bar what is low compared to the pressure variations observed between two iterations.

5.3 Solutions

In this paragraph, we detail the various ways that were studied to improve the code stability. The β coefficient is a fixed parameter calculated using the following formula:

$$\beta^2 = \beta_0^2 U_{ref}^2 \text{ where } \beta_0^2 = 3 \text{ and } U_{ref} \text{ is a reference velocity}$$

Consequently, we initially tried to decrease the reference velocity value. Generally, it is recommended to use the highest velocity of the flow in order to maximize artificial dissipation. Initially, we decided not to modify the calculation of the spectral radius in order to preserve high levels of dissipation. Stability was indeed improved but the results obtained were characterized by very bad convergence level (2% of error on the mass flow conservation) and by cavity shapes far from being probable.

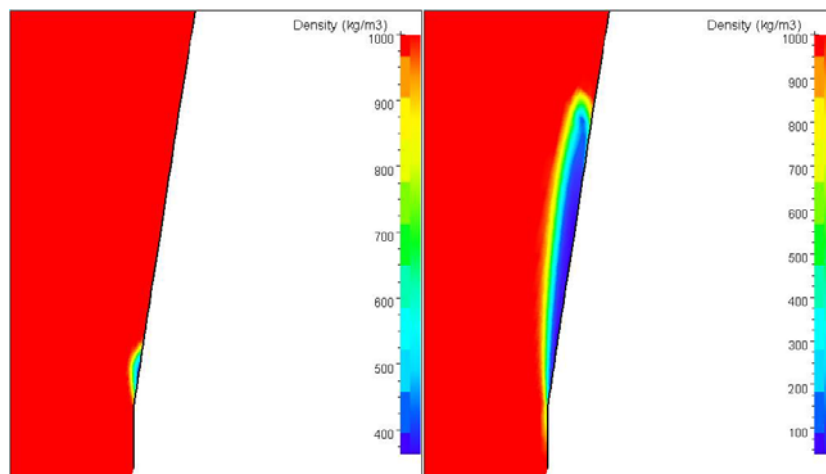


Figure 5.2: influence Dissipation on the Cavity Shape.

The increase in dissipation generates a reduction of cavity length associated with a very strong smoothing of the interface. Consequently, we decided to modify the calculation of the spectral radius in a coherent way with the reduction of β and a great improvement was observed. Then, in order to minimize the computing time, we decided to limit the influence of the β reduction in cavitating areas. Finally, we defined a β law depending on static pressure.

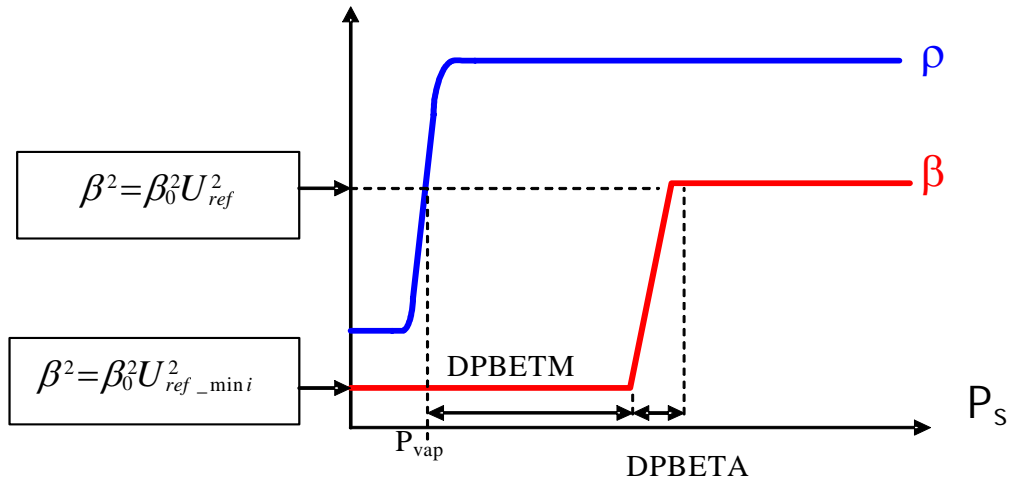


Figure 5.3: Evolution of β versus Static Pressure.

Linking between the minimum and maximum value of β is made outside from the barotropic state law in order to stabilize the evolution of the cells where pure liquid is converted into vapour. This law has provided high stability to the algorithm.

5.4 Influence of State Law Parameters

We are mainly interested in the influence of the parameters of the state law : RHOV and AMIN. It is important to keep in mind that RHOV should not be considered as the vapour density value but rather as the minimal density value of the mixture; thus, a value of 100 for cold water means that the maximum void fraction value that we can simulate is 90 %, which is higher than the maximum void fraction values measured in a venturi.

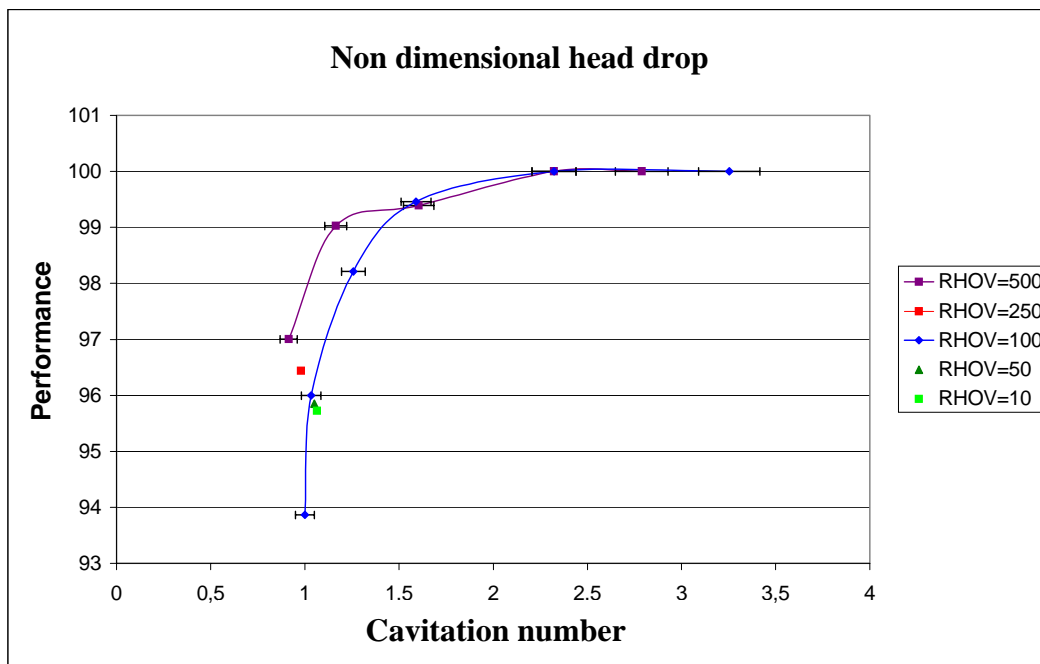


Figure 5.4: RHOV Influence.

The value of 500 allows to predict a head drop whose uncertainty is about 10 %. On the other hand, the operating point calculated with RHOV=50 is very close to that calculated for RHOV=100 (deviation lower than 2%).

The study of the AMIN influence was also led on this geometry for values going from 30 to 100. No effect could be observed on the total performance of the impeller. However, we observed a significant dependence of the cavity volume on this parameter. For example, a variation of AMIN from 35 to 75 led to an increase of cavity thickness of about 20 %.

6.0 HEAD DROP OF IMPELLERS

SHF impeller was designed by NEYRPIC company in the frame of a research project on partial flow rates operation. This impeller was tested at ENSAM Lille in air, at INSA Lyon, EPF Lausanne and HYDROART Milan in water. Numerical studies were also performed by Combes [2]. The main characteristics of SHF impeller are:

- A number of blades: 7.
- Number of revolutions: 3000 tours/min.
- Nominal capacity: 0,157 m³/s.
- Diameter piping upstream: 200mm.
- Diameter left: 330 mm.

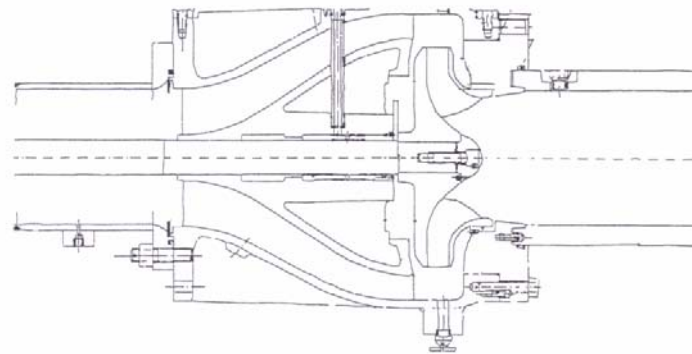


Figure 6.1: SHF Pump.

6.1 Mesh and Cutting Plans

In this paragraph, we quickly recall the main characteristics of the mesh that is used for the calculations.

- Size of first cell near a wall = 10 μm .
- Additional refinement at leading edge with an expansion coefficient of 0.3.
- 10 cells without size variations in the center of the channel in azimuth direction.
- 12 cells without size variations in the center of the channel in radial direction.

Total number of internal nodes is 250000 ; this value has been chosen after a mesh convergence based on computations with other meshes of 170 000, 500000 and 1000000 nodes. The boundary conditions are: imposed velocity at inlet, imposed static pressure at outlet, and periodicity conditions.

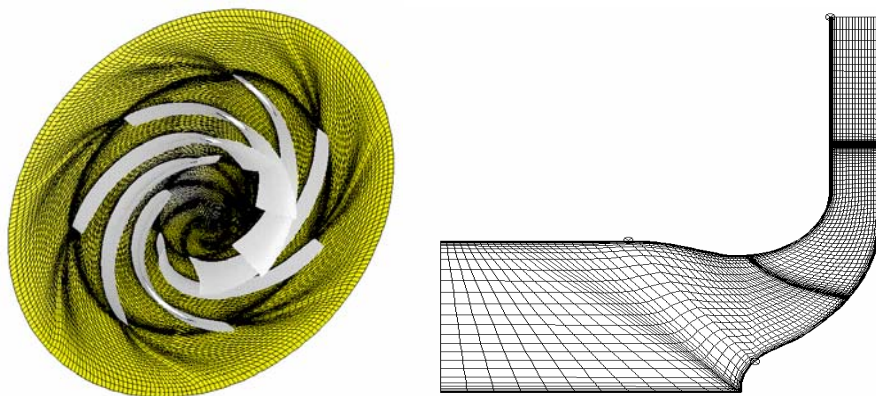


Figure 6.2: 3d and Meridian View of the Mesh.

To study the local flow structures, we created cutting plans orthogonal to the meridian direction. All the results will be presented with the following conventions:

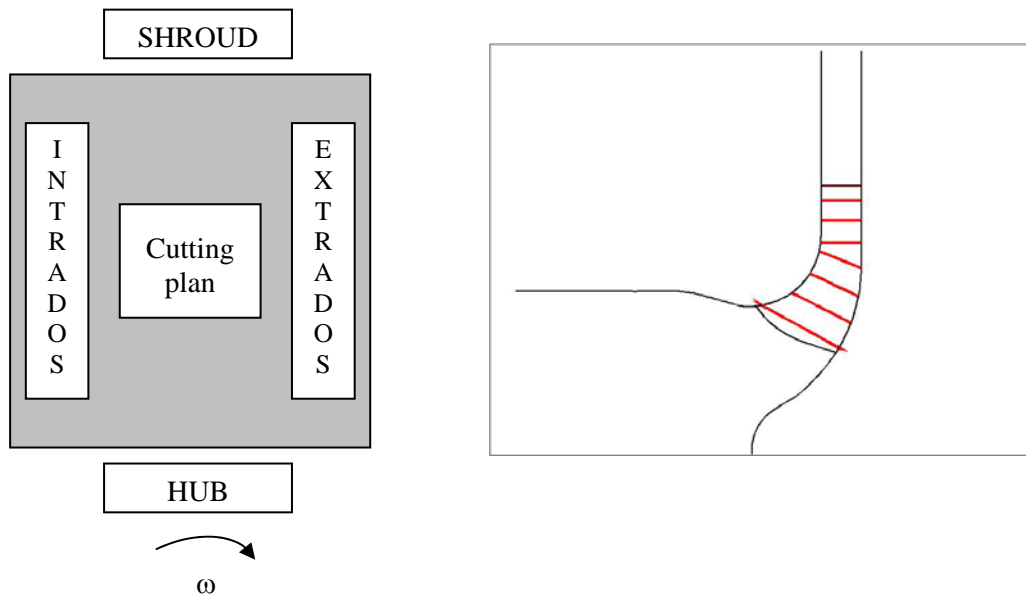


Figure 6.3: Cutting Plans.

The plans are numbered from I to VIII from inlet to outlet. Shape of the plans is very distorted due to high twisting of the blades.

6.2 Cavitating Results

The presentation of the cavitating results is carried out in two steps: first of all, we explain the head drop phenomenon from a global point of view and then, we expose some local modifications induced by the development of the cavitation sheets.

6.2.1 Global Results

First, we expose the elements explaining the head drop phenomenon. For that, we first present the head drop curves that we obtained for various flow rates:

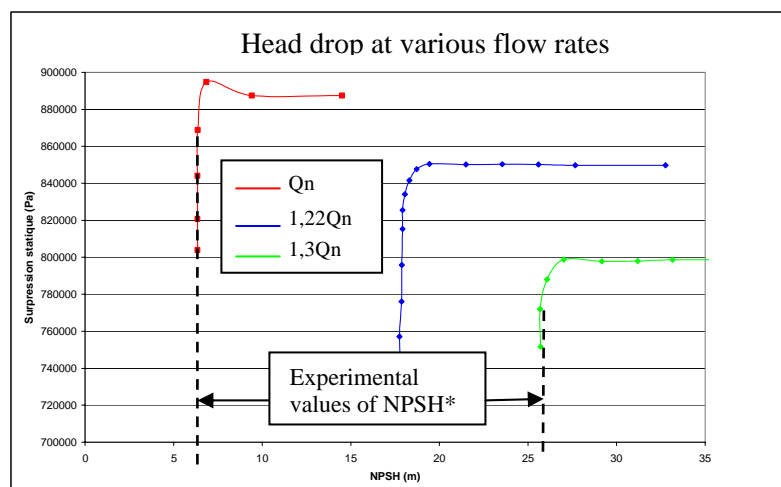


Figure 6.4: Head Drops for Various Mass Flows.

Numerical Modelling of Cavitation

Head is here defined as the static pressure rise between inlet and outlet sections. The last converged point corresponds to a 10 % head drop. Moreover, one will note that the calculated value of NPSH corresponding to head drop is constant four different calculations, which is a sign of good convergence. Last, the good agreement with measured value has to be noticed. Next, we examine the evolution of cavitation for decreasing σ values.

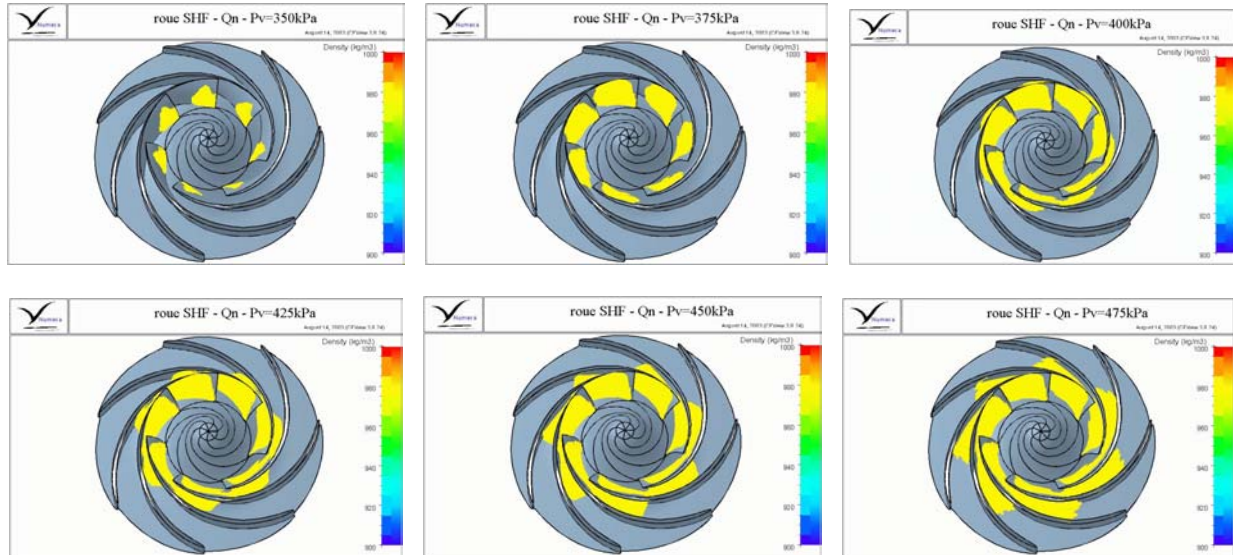


Figure 6.5: Evolution of the Cavities.

The cavity appears initially on suction side near the hub. It develops mainly in radial and meridian directions until reaching the throat, which provokes the brutal performance drop. Lastly, cavitation develops on pressure side very close to the shroud; then an important azimuth and radial extension is observed. The two cavities (suction face and shroud) are very thin.

With regard to the head drop of the machine, it is interesting to dissociate the energy transfer and the losses. Consequently, we present the respective evolutions of the hydraulic and mechanical power.

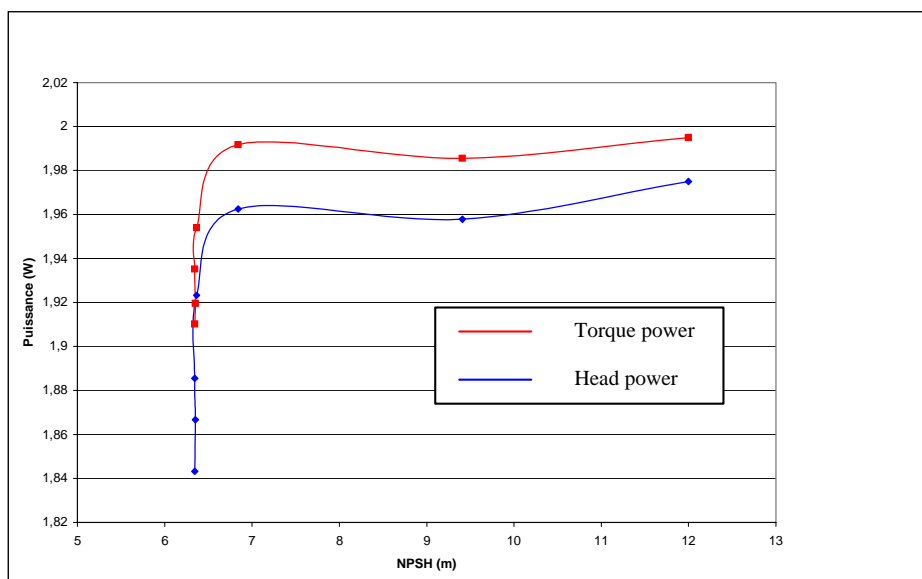


Figure 6.6: Hydraulic and Mechanical Power Evolution.

Thus, it appears that hydraulic and mechanical power decrease almost simultaneously, which means that the decrease in pressure rise is mainly due to a reduction of the torque. Loss of efficiency can be seen as a second order as the decrease is about 2 % for the last cavitating point, which is negligible in front of the torque reduction. In order to have a better understanding of this evolution, we compare the blade load at mid span for various values of NPSH.

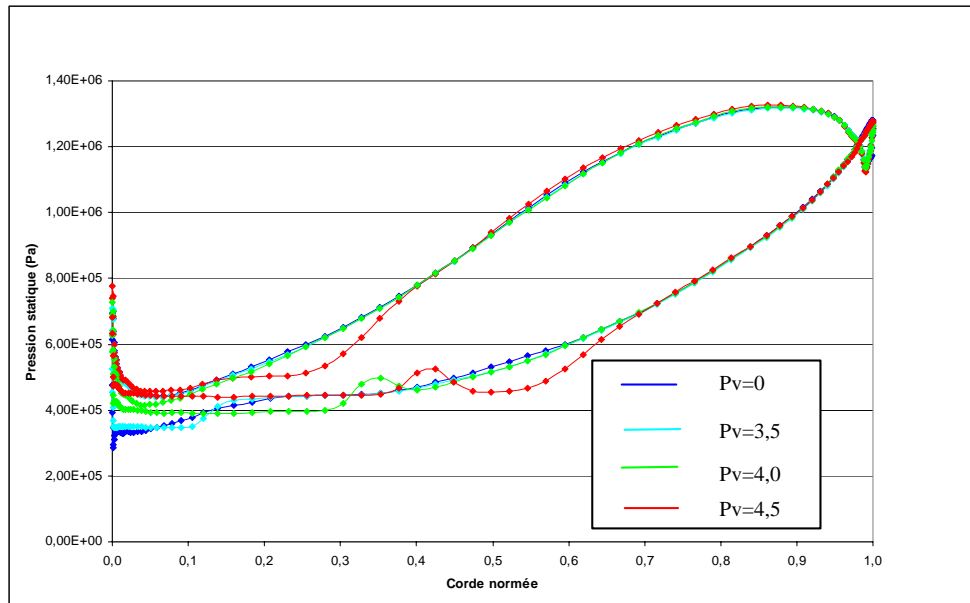


Figure 6.7: Load Evolution at Mid Span.

The development of cavitation corresponds to the evolution from blue to red. Thus, it is noted that the torque reduction is connected very simply to the growth of the cavity. Static pressure is limited to vapour pressure whereas one would need lower pressure to preserve the same blade load. Moreover, these curves highlight an increase in the load downstream from the cavity.

Next, it is interesting to examine how these modifications of the blade loading change the energy transfers inside the machine.

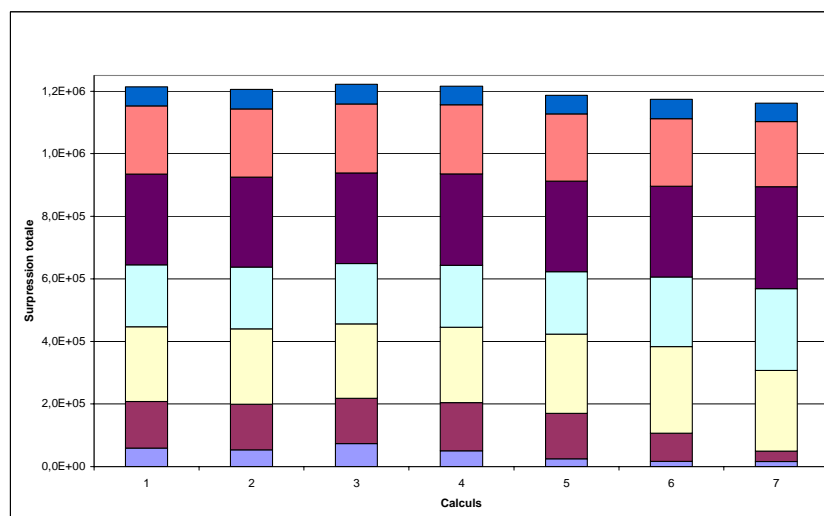


Figure 6.8: Evolution of Internal Pressure Rises.

Each histogram element represents the total pressure rise of the impeller for a particular calculation. Calculation 1 is calculation without cavitation and calculation 7 is the calculation carried out with the lowest sigma value. Total pressure rise is then distributed in 7 portions corresponding to the 7 intervals between the cutting plans defined on figure 6.3.

This representation highlights the meridian evolution of total pressure rise:

- In the first portion (violet colour), one observes for the first three operating points an increase in the total pressure rise that causes a global performance increase. This phenomenon can be explained by an incidence effect: the development of the cavity thickens the suction side profile inducing a local increase in the incidence.
- A compensation phenomenon is observed downstream from the cavitation sheet. This phenomenon is particularly visible in portion 4 (light blue) for calculations 4 to 7.

6.2.2 Local Results

In this part, we are interested in the modifications of the flow induced by the development of a cavitation sheet. We use the cuts defined on figure 6.3. Our study is limited to the comparison of non dimensional relative helicity for the most developed cavitating configuration (NPSH \approx 6,3m).

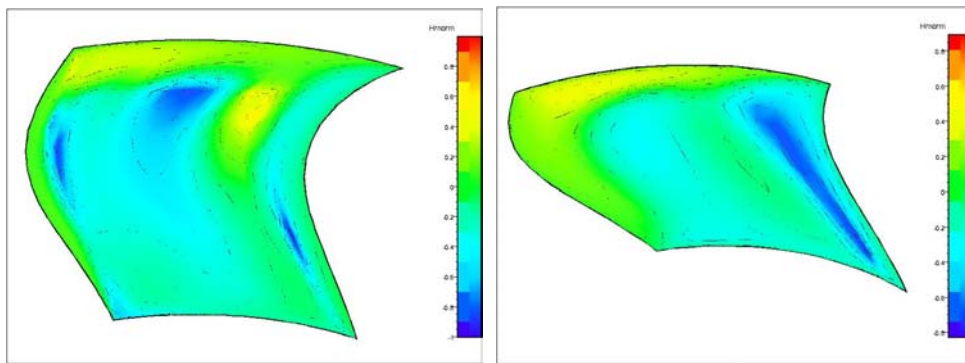


Figure 6.9: Non Dimensional Relative Helicity in Plans I and II (Non Cavitating).

In plan I, the flow seems very heterogeneous and it is difficult to give an interpretation of the structures observed. In plan II, one observes the development of the first secondary flows. Thus, the effect of meridian curvature is particularly visible near the suction side. On the pressure side, the swirling structure develops with difficulty and remains confined near the shroud.

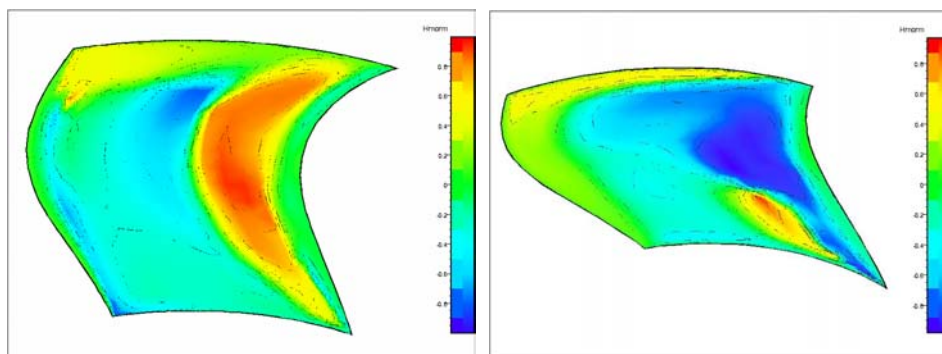


Figure 6.10: Non Dimensional Relative Helicity in Plans I and II (Cavitating).

The observation of the non dimensional relative helicity in plan I illustrates a very significant modification of the secondary flows. In non cavitating configuration, it was difficult to distinguish organized structures whereas the presence of the cavity generates a swirling zone near the interface. In plan II, one notes that the structure observed in plan I almost disappeared and that it persists only near the hub. On the other hand, one notes the development of a major swirling structure near the suction side whose presence may be explained by the centrifugation of the wake of the cavity.

7.0 HEAD DROP OF INDUCERS

This part is devoted to the simulation of cavitating flows in two rocket engine inducers.

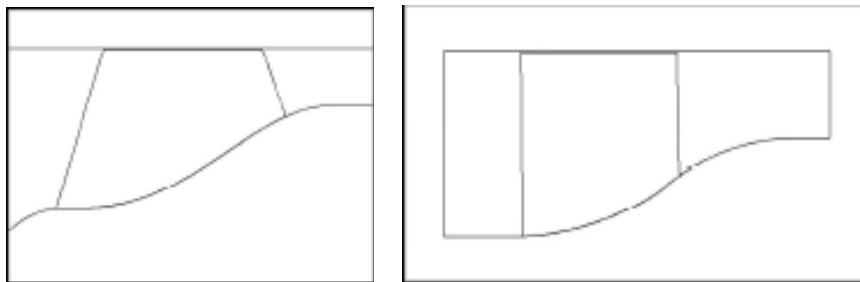


Figure 7.1: inducer Geometries (left = Inducer 1 and right = Inducer 2).

Both inducers were designed for research objectives ; the first inducer was designed by Snecma and the second inducer was designed by Pr. Tsujimoto team from Osaka University.

7.1 Inducer 1

7.1.1 Mesh and Cutting Plans

In this paragraph, we quickly recall the main characteristics of the mesh that is used for the calculations.

- Size of first cell near a wall = 5 μm .
- 41 cells in azimuth direction.
- 41 cells in radial direction.
- 203 cells in axial direction.

Total number of internal nodes is 350000 for one blade to blade channel; this value has been chosen after a mesh convergence based on computations with other meshes up to 1000000 nodes. The boundary conditions are: imposed velocity at the mesh inlet, imposed static pressure at the outlet, and periodicity conditions. The turbulence models is standard k- ϵ with wall functions. Tip gap has been taken into account only for mesh convergence in non cavitating conditions. Numerical results were validated by comparison with experimental results on static pressure evolution on the shroud for non cavitating conditions.

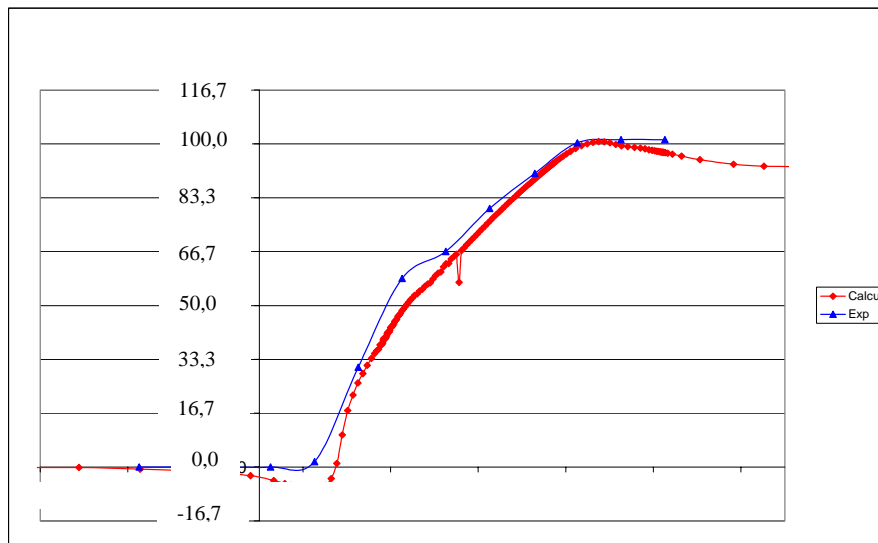


Figure 7.2: Evolution of Static Pressure vs Axial Length.

To study the local flow structures, we created cutting plans orthogonal to the meridian direction. All the results will be presented with the following conventions:

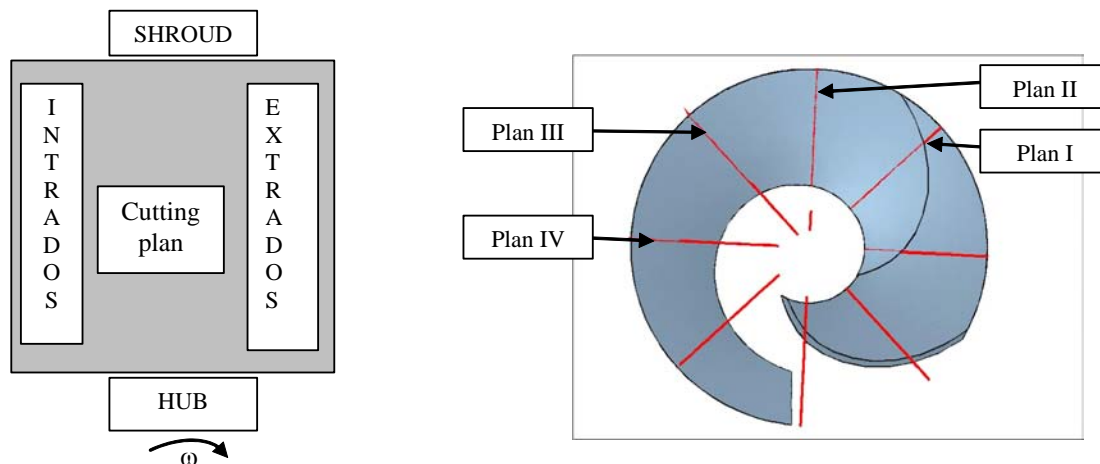


Figure 7.3: Cutting Plans.

7.1.2 Cavitating Results

The presentation of the cavitating results is carried out in two steps: first of all, we explain the phenomenon of head drop from a global point of view and then, we expose the local modifications induced by the development of the cavitation sheets.

7.1.2.1 Global Analysis

First, we expose elements related to head drop phenomenon.

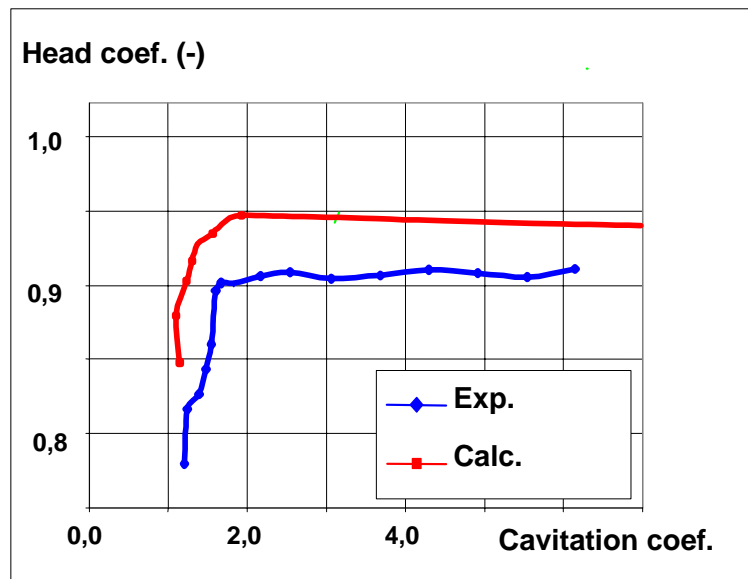


Figure 7.4: Head Drop at Nominal Flow Rate.

Concerning the prediction of sigma value associated with head drop, a good agreement between numerical and experimental values is obtained. The brutal behaviour of the head drop is also well described. The absolute head gap can be explained by our neglecting the tip gap in these calculations.

Next, we examine the evolution of cavitation for decreasing σ values.

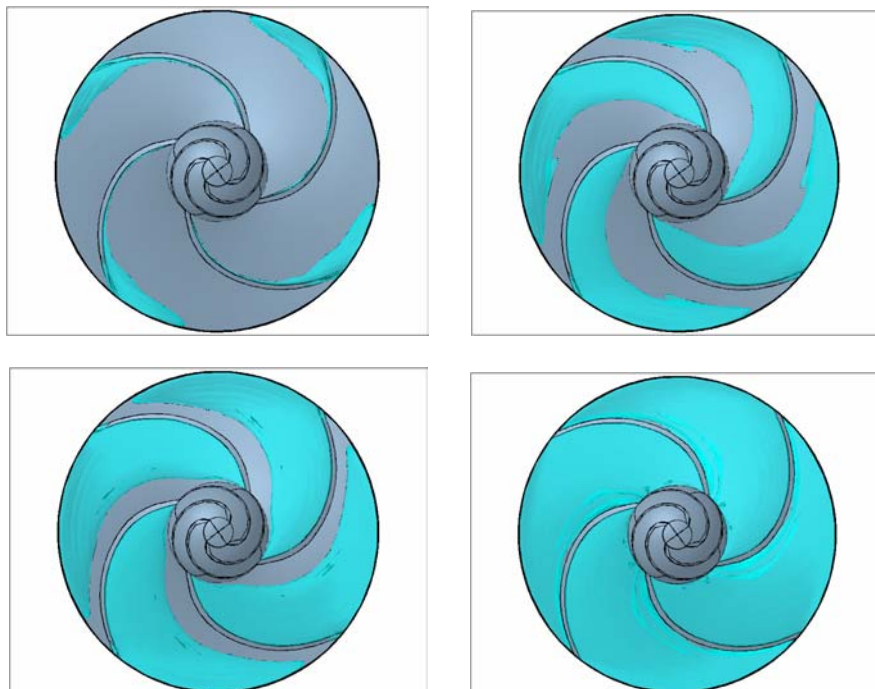


Figure 7.5: Evolution of the Cavity.

Cavitation appears initially near the shroud on the suction side and remains very localised for a wide range of σ values. Then, cavitation mainly develops in the back flow creating a highly three-dimensional

structure near the shroud. One then attends the appearance of a cavity attached to the leading edge along the span of the blade. This cavity grows mainly in the meridian direction. It will be noted in addition that the thickness of the cavities is low and that spanwise extension remains rather uniform. Then, we present the evolution of hydraulic and mechanical power.

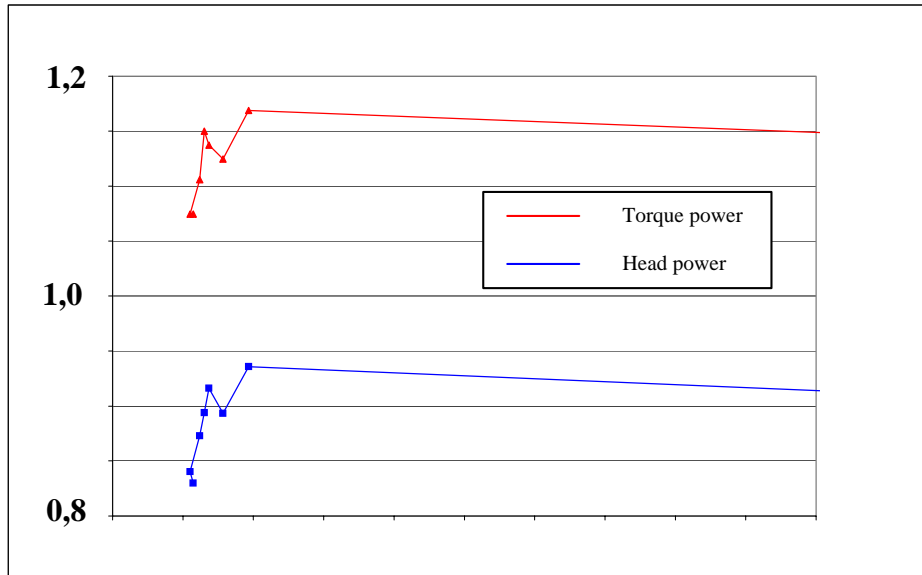


Figure 7.6: Evolution of Hydraulic and Mechanical Power.

It appears that the drops of hydraulic and mechanical power are almost simultaneous, which means that the decrease in pressure rise is mainly due to a reduction of the torque like for the SHF impeller. The fall of efficiency is about 3 % for the last calculated point.

In order to have a better understanding of this evolution, we compare the blade load at mid span for various sigma values.

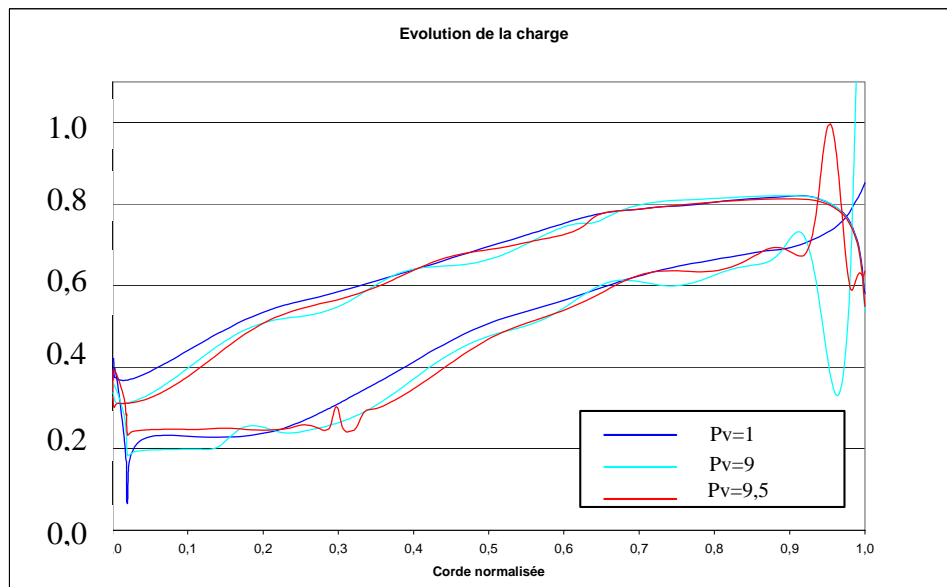


Figure 7.7: Evolution of the Blade Load.

The development of cavitation corresponds to the evolution from blue to red. Thus, it is noted that the torque reduction is connected as for the SHF impeller to the growth of cavity length. Static pressure is limited to vapour pressure whereas lower pressures are needed to preserve the same blade load. On the other hand, the effects of compensation observed on the load profiles for SHF impeller are not obvious here. Moreover, contrarily to what was observed on SHF impeller, one notes a significant modification of the static pressure profile on pressure side that is responsible for part of the head drop. Next, it is interesting to examine how these modifications of the blade loading change the energy transfers inside the machine.

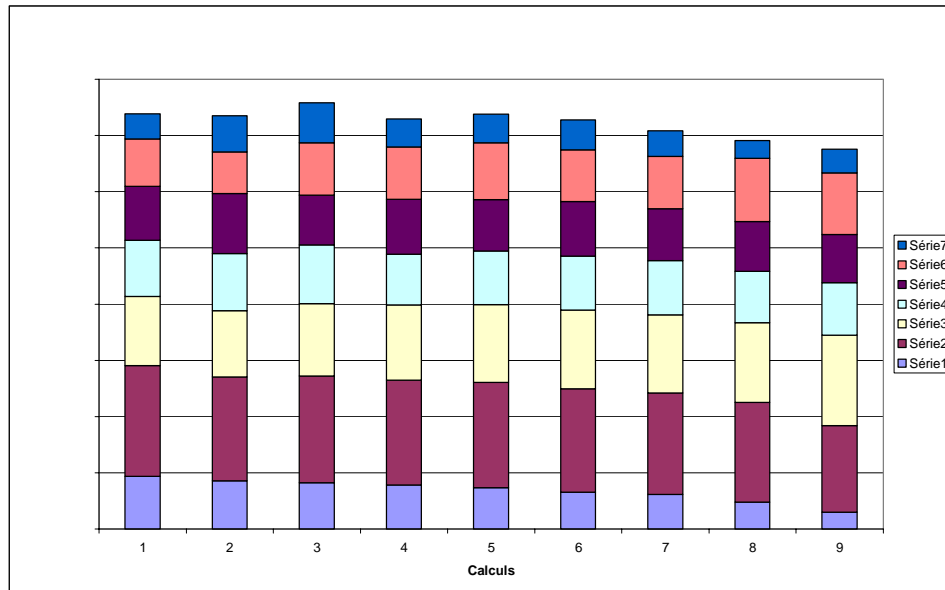


Figure 7.8: Evolution of Internal Pressure Rises.

Each element of the histogram represents the total pressure rise of the inducer for a particular calculation. Calculation 1 is performed in non cavitating conditions and calculation 9 is the calculation carried out with the lowest sigma value. Total pressure rise is then distributed in 7 portions corresponding to the 7 intervals between the cutting plans defined on figure 7.3. This representation highlights the meridian evolution of total pressure rise:

- In the first portion (violet colour), the pressure rise increase observed on the SHF impeller for the highest sigma values doesn't appear.
- In the second portion, one observes for the second point a decrease of pressure rise that is responsible of the global pressure rise decrease observed on the inducer at this point. Indeed, it is noted that the pressure rise provided by other portions is not affected.

Finally, as it was said by examining the load profiles, this study confirms that the compensation phenomena observed on SHF impeller don't exist in this inducer.

7.1.2.2 Local Analysis

In this part, we focus on the modifications of the flow induced by the development of a cavitation sheet. We use the cutting plans presented on figure 7.3 to visualise axial velocity and non dimensional relative helicity distributions.

- Axial velocity :

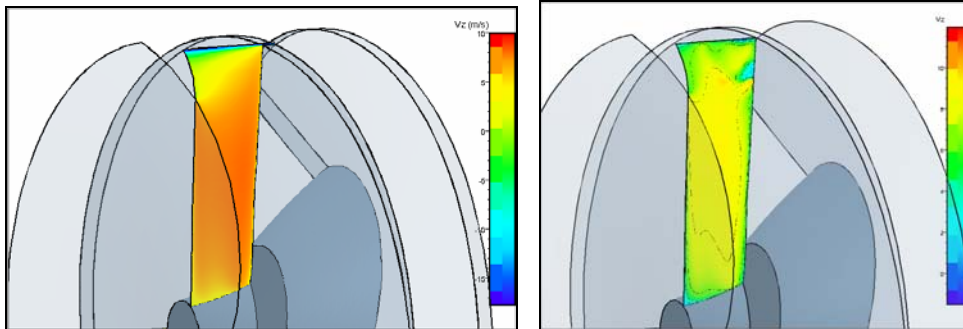


Figure 7.9: Axial Velocity in Plan I (left = Non Cavitating, right = Cavitating).

In plan I, one notes that the presence of the cavity generates heterogeneities in the axial velocity distribution. In particular, one will note the presence of low velocity zones on suction side that are due to the obstruction generated by the cavity. In plan II, we could observe that the flow remains very homogeneous.

- Secondary flows:

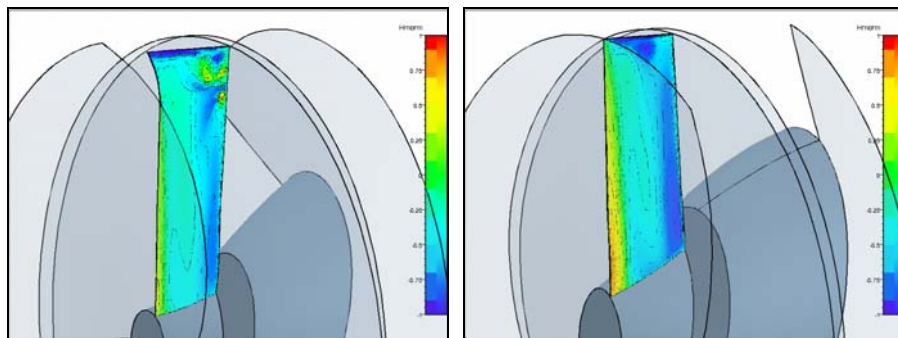


Figure 7.10: Distribution of Relative Helicity in Plans I and II (Cavitating).

In plan I, the distribution of non dimensional relative helicity is very disturbed on suction side near the shroud. This phenomenon can be explained by the presence in this zone of the wake of the cavity. Near the hub, the secondary flows are close to those observed in non cavitating calculations.

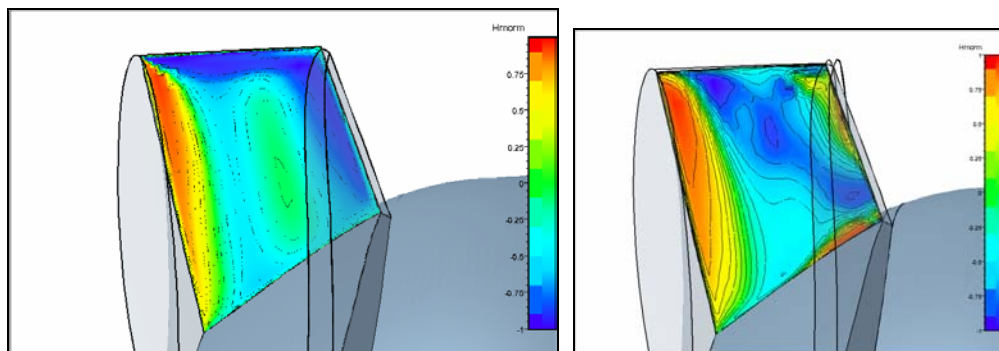


Figure 7.11: Distribution of Relative Helicity in Plan IV (left = Non Cavitating, right = Cavitating).

In plans II and III, we noted that the pressure side and suction side vortices were very close to those observed in non cavitating computations. In plan IV, significant differences have been seen with non cavitating distribution. For example, we could observe that the pressure side vortex deeply modified the suction side flow near the trailing edge. Indeed, one notes disappearance on this face of the negative helicity structure that was convected towards the centre of the channel. Lastly, one also raises the existence of a small structure near the hub that didn't exist in non cavitating computation. Consequently, it has to be reminded that the outlet flow is highly disturbed by the development of the cavity.

7.2 Inducer 2

7.2.1 Mesh and Cutting Plans

In this paragraph, we quickly recall the main characteristics of the mesh that is used for the calculations.

- Size of first cell near a wall = 10 μm .
- 41 cells in azimuth direction.
- 41 cells in radial direction.
- 149 cells in axial direction.

Total number of internal nodes is 250000 for one blade to blade channel; this value has been chosen after a mesh convergence based on computations with other meshes whose cells number was up to 500000. The boundary conditions are: imposed velocity at inlet, imposed static pressure at outlet, and periodicity conditions. The turbulence model is standard k- ϵ with wall functions. Tip gap has not been taken into account.

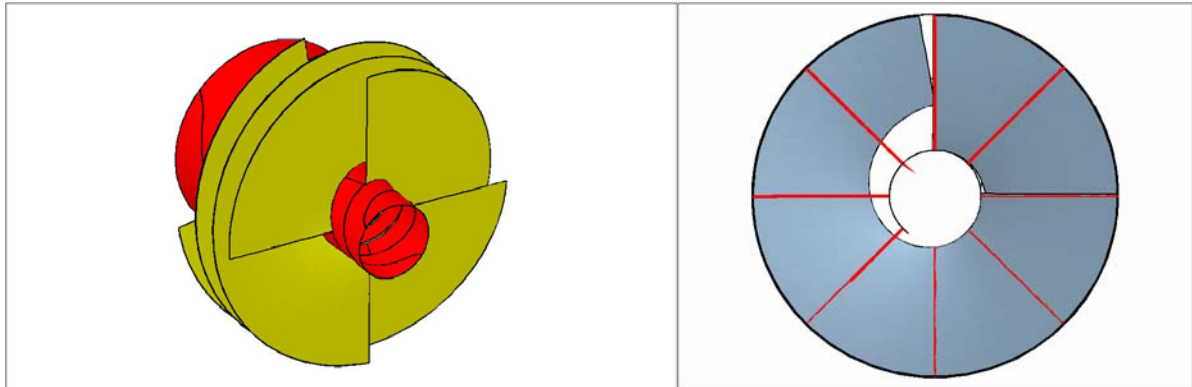


Figure 7.12: Geometry and Definition of Cutting Plans.

7.2.2 Cavitating Results

The presentation of the cavitating results is focused on the head drop phenomenon. We first recall the head drop curve that was obtained at nominal flow rate.

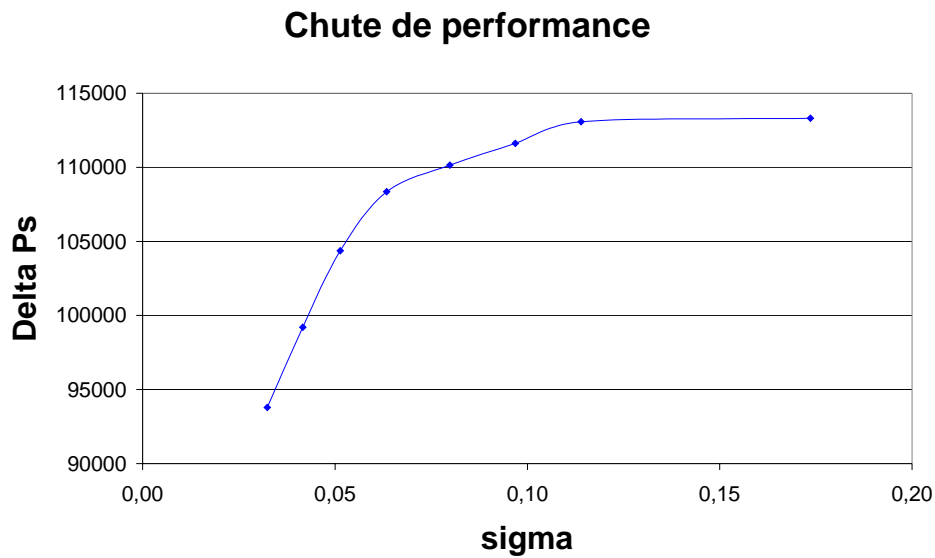


Figure 7.13: Head Drop.

We then examine the evolution of cavitation for various sigma values.

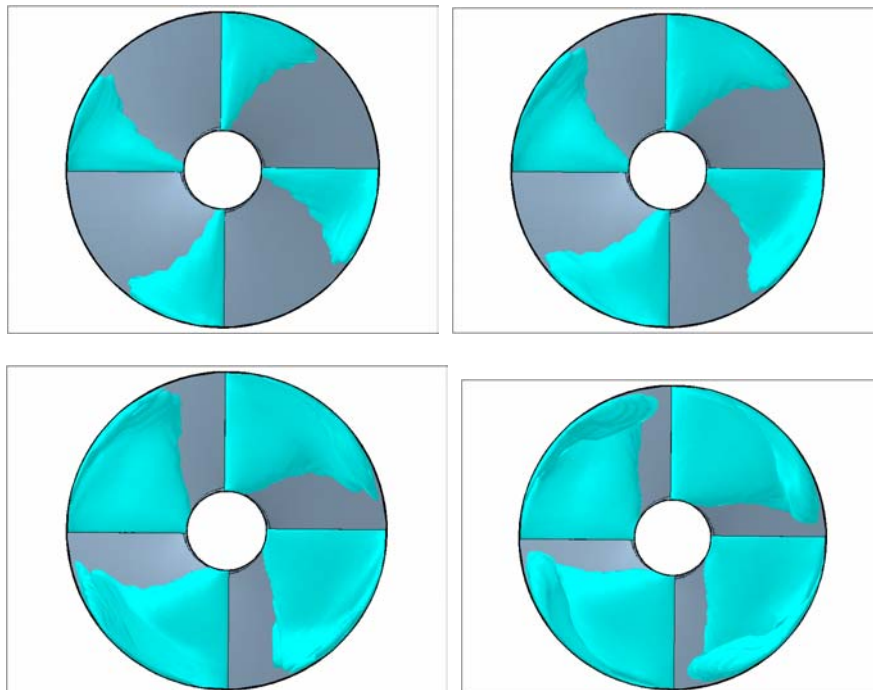


Figure 7.14: Evolution of the Cavities.

Cavitation appears on all the height of the blade with a triangular shape whose base is on the shroud. This cavity grows uniformly when decreasing the σ value. Cavitation develops in the back flow, which creates a highly three-dimensional diphasic structure near the shroud and extending upstream. Cavitation sheets are thicker than for inducer 1.

To characterize the performance drop, we examine the evolution of hydraulic and mechanical power.

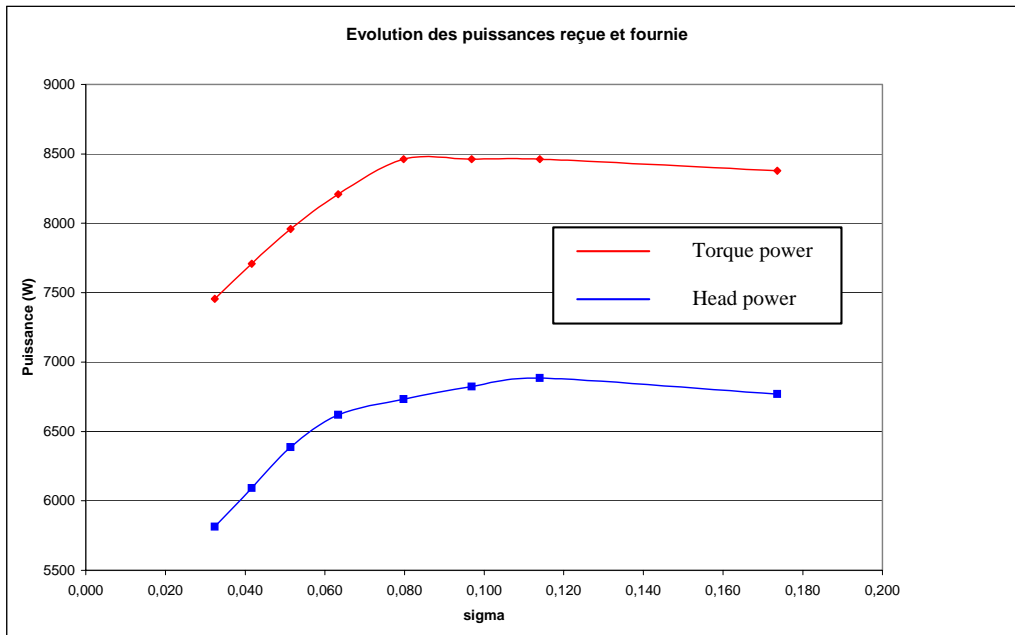


Figure 7.15: Evolution of the Hydraulic and Mechanical Power.

It appears that the hydraulic and mechanical power drops are almost simultaneous, which means that the decrease in pressure rise is mainly due to a reduction of the torque like for the SHF impeller. The efficiency loss is about 3 % for the last calculated point. These results are identical to what has been seen on inducer 1.

In order to have a better understanding of this evolution, we compare the blade load at mid span for various sigma values.

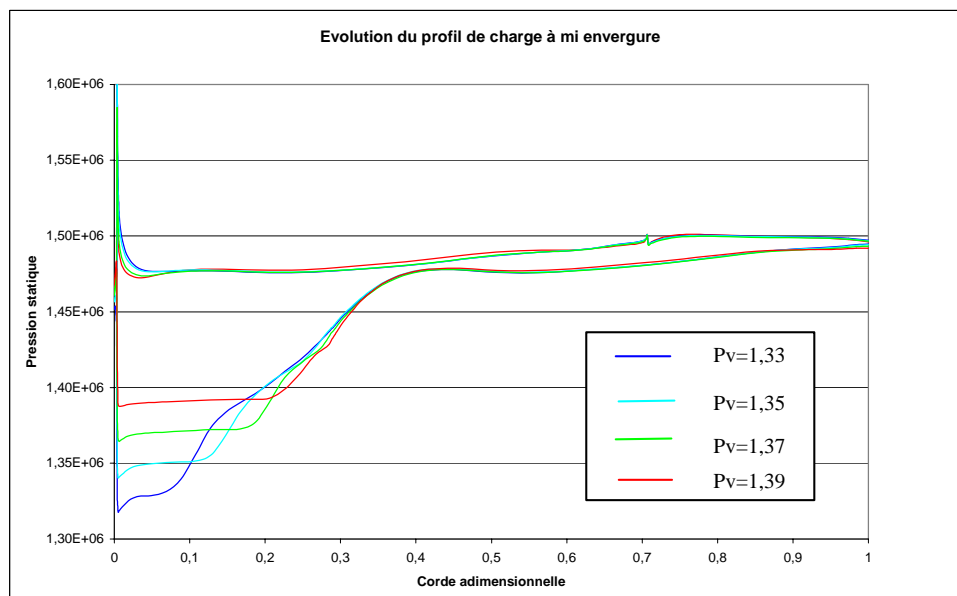


Figure 7.16: Modification of the Blade Load at Mid Span.

The development of cavitation corresponds to the evolution from blue to red. Thus, it is noted that the torque reduction is connected as for SHF impeller and inducer 1 to the growth of cavity length. Static pressure is limited to vapour pressure whereas lower pressures are needed to preserve the same blade load. The compensation effects observed downstream from the cavity for SHF impeller are lower on inducer 2 than on SHF impeller. This effect didn't exist on inducer 1; this difference is explained by the fact that pressure side profile isn't modified contrarily to what was observed on inducer 1. This evolution of the load also explains why the head drop of the inducer 1 is so progressive: this inducer was dimensioned with high incidence angles, which results in high loading of the first part of the blade. Consequently, appearance of cavitation in this area generates a torque drop that cannot be compensated. Next, it is interesting to examine how these modifications of the blade loading change the energy transfers inside the machine.

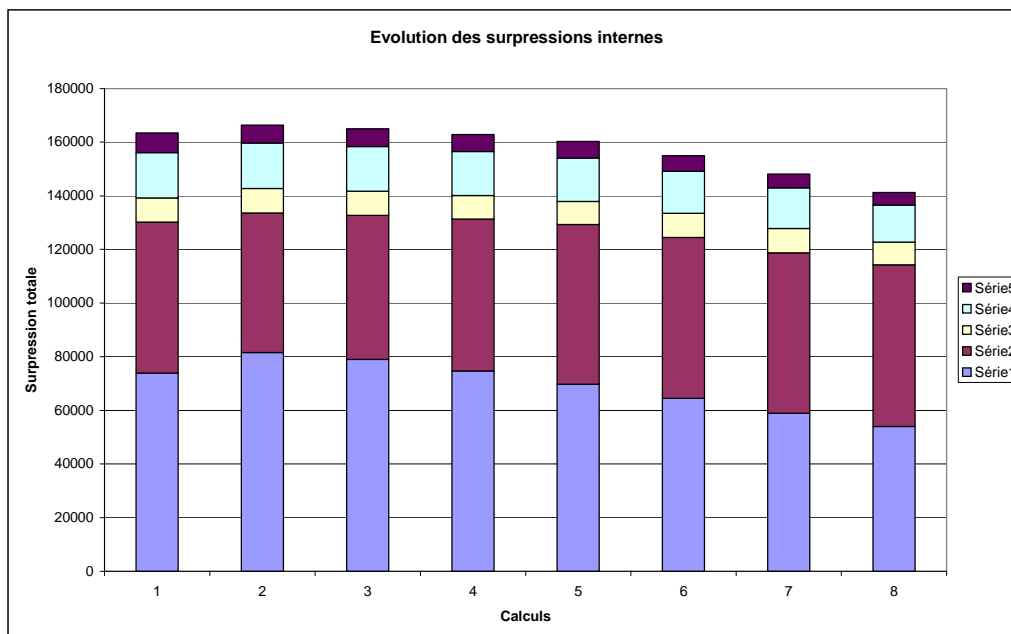


Figure 7.17: Evolution of Internal Pressure Rises.

Each element of the histogram represents the total pressure rise of the inducer for a particular calculation. Calculation 1 is calculation without cavitation and calculation 8 is the calculation carried out for the lowest sigma value. Total pressure rise is then distributed in 5 portions corresponding to the 5 intervals between the cutting plans defined on figure 7.12. This representation highlights the axial evolution of total pressure rise:

- The incidence loading is clearly highlighted on the energy transfers histograms since one can note that the transfers taking place in the last three sections are weak in front of those in the first two sections.
- In the first section, a pressure rise increase is observed while cavitation is developing. This is similar to what was found on SHF impeller.
- The compensation phenomenon observed downstream from the cavity on the load profiles is very clear when comparing the evolution of the first two sections.

8.0 INSTABILITIES IN A CASCADE

This last part of the note is devoted to the presentation of some numerical simulation of cavitation instabilities in a 2D blade cascade.

8.1 Presentation

To obtain the 2D geometry, a 3D inducer is cut at a constant radius R_c equal to 70% of the tip radius R . The boundary conditions are: imposed velocity at inlet, imposed static pressure at outlet, and periodicity or connection conditions between the different channels of the blade cascade. The time step, mesh and turbulence model are chosen to put the attention on the low frequency fluctuations of the attached cavity, more than on the local unsteadiness in the cavitation sheet wake (cloud shedding).

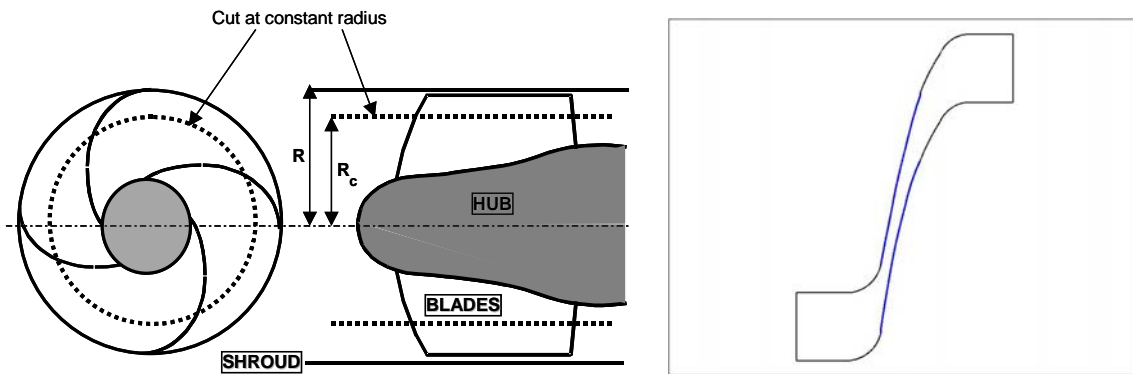


Figure 8.1: Cascade and Mesh Topology.

A non cavitating mesh convergence was performed on the following grids: m0: 329*61, m1: 625*121, m2: 625*101, m3: 625*81, m4: 625*61, m5: 625*41, m6: 585*81 and m7: 841*201. The first number is the axial number of cells and the second number is the number of cells in the azimuth direction. We concluded that mesh convergence was obtained with m4 grid.

8.2 Steady Cavitating Results

First, we present the computation of head drop at nominal flow rate.

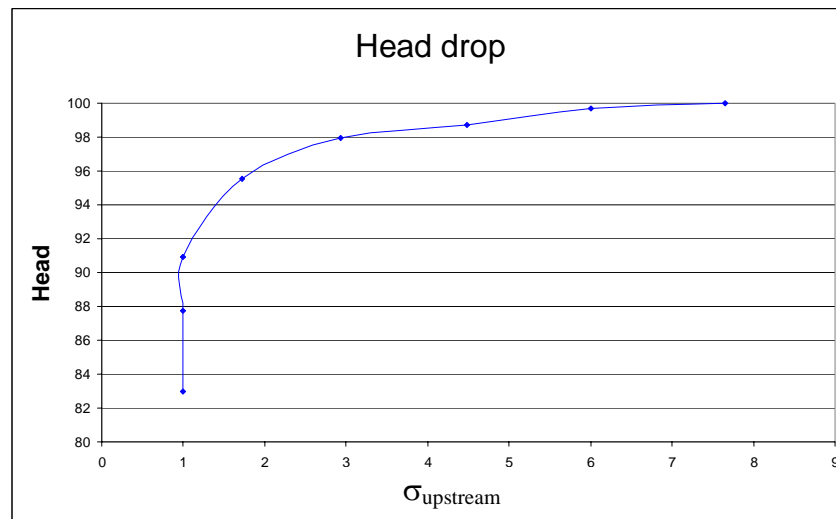


Figure 8.2: Head Drop Curve.

The non dimensional head is defined as the static pressure rise between inlet and outlet sections divided by the non cavitating value. The last converged point corresponds to a head drop of 17 %.

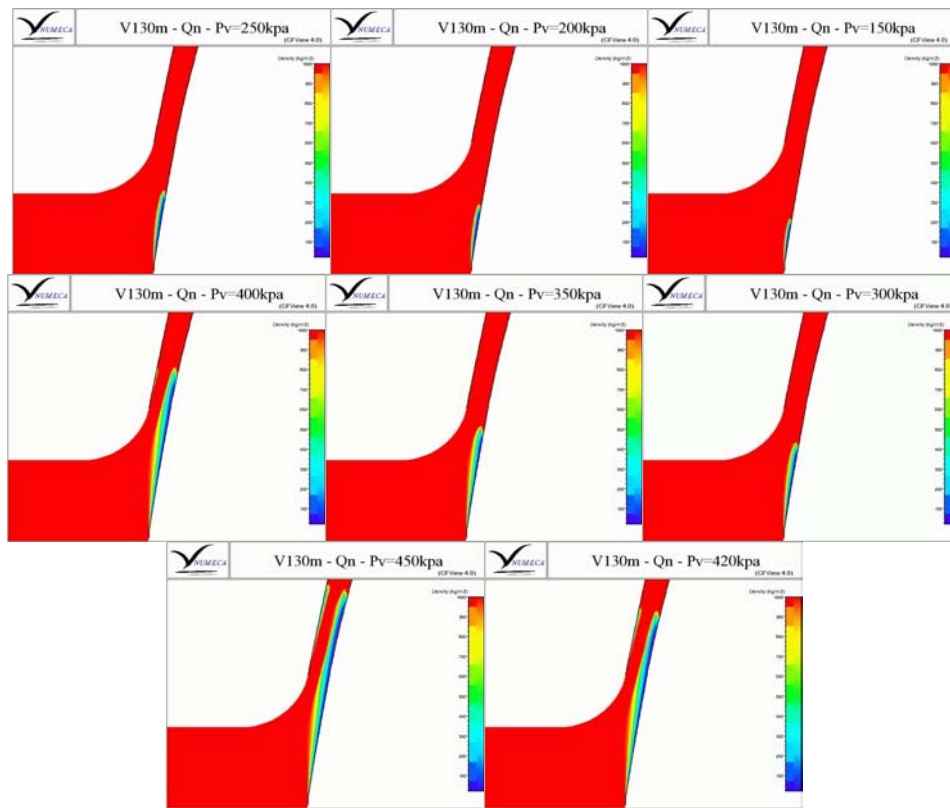


Figure 8.3: Evolution of the Cavity.

As long as the cavity length remains lower than half of the distance between the leading edge and the throat, the head drop remains lower than 1 %. Moreover, the brutal head drop appears only when the cavity reaches the throat. This result will be analyzed thereafter. Lastly, it will be observed that the appearance of cavitation on pressure side takes place at the same instant, which is coherent with the results that we obtained on other geometries (SHF impeller for example). Hydraulic and mechanical power drops are almost simultaneous as it was already observed on SHF impeller and on the two inducer geometries. The loss of efficiency reaches 5,5 % for these simulations. As for the 3D geometries, we examine the evolution of blade load for various σ values:

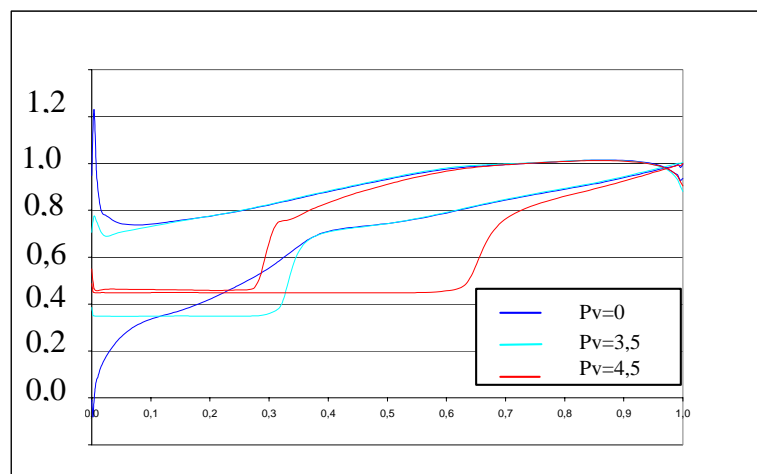


Figure 8.4: Evolution of the Blade Load.

The cavitation development corresponds to the evolution from blue to red. The performance drop of the cascade is directly related to the blade loading: the appearance of cavitation on the pressure side leads to a torque decrease and then to the performance drop. With regard to the effects of compensation, they intervene here in a rather significant way downstream from the cavity.

8.3 Unsteady Cavitating Results

In this part, we present our simulations of cavitation instabilities.

8.3.1 Calculation Parameters

The mesh that has been used for unsteady cavitating calculations is a rather coarse grid (215*31) in order to minimize the computing time ; the error induced is about 10 % on absolute non cavitating pressure rise but it is negligible regarding the prediction of head drop sigma value. Four channels have been meshed since we intend to simulate dissymmetrical phenomena:

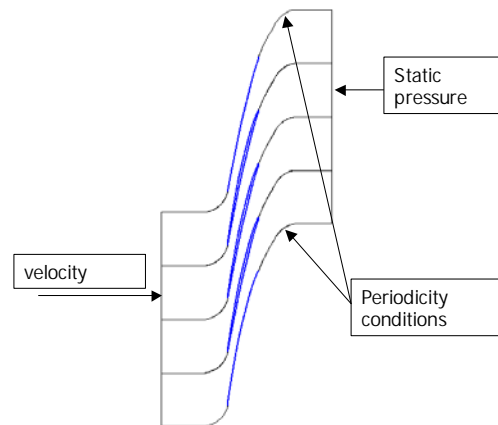


Figure 8.5: Mesh Topology for Unsteady Calculations.

8.3.2 Instability Configurations

Several four-channels computations are performed at nominal flow rate, for different outlet cavitation number σ varying from low cavitating conditions down to the final performance drop. The corresponding head drop chart is drawn in Figure 5 at nominal flow rate.

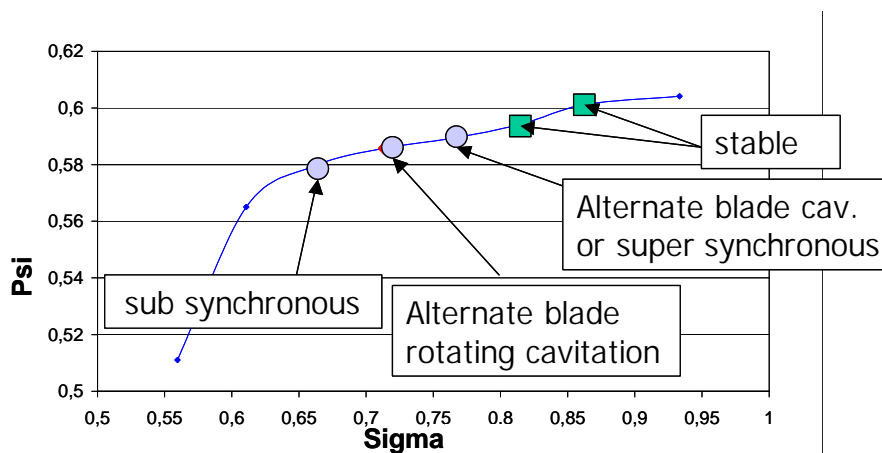


Figure 8.6: Calculated Points of Operation.

Stable configurations correspond to cavitation numbers lower than 0.65 or higher than 0.8 (square dots in the figure). For $\sigma > 0.8$, sheets of cavitation are small and identical in the 4 channels. For these flow conditions, the performance of the runner is only slightly affected by the presence of vapour. For $\sigma < 0.65$, the cavitation sheets are much more developed, and they are responsible for the important performance drop observed.

Calculations are done in relative referential: sub or super synchronous configurations are determined by the sheets visualization. For example, if the sheet configuration rotates in the same direction as the inducer, the characteristic frequency of the instability is added to the inducer rotation frequency and a super synchronous configuration is established. In another way, sub synchronous regimes are characterized by cavitation patterns that rotate in the opposite direction as the inducer.

8.3.2.1 Super Synchronous Configuration

The super synchronous configuration appeared for a σ_{upstream} value of 0,75.

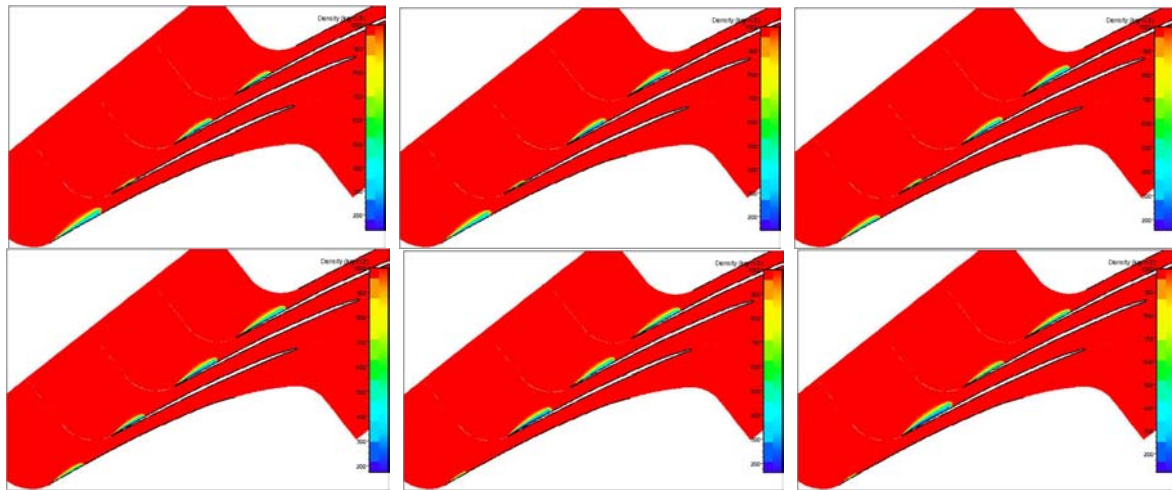


Figure 8.7: Evolution of the Cavitation Sheets.

The super synchronous configuration is characterized by the rotation of a small cavity in the rotating direction of the inducer.

8.3.2.2 Sub-Synchronous Configuration

The sub-synchronous configuration appeared for a σ_{upstream} value of 0,65; when a cavity was big enough to block a blade to blade channel:

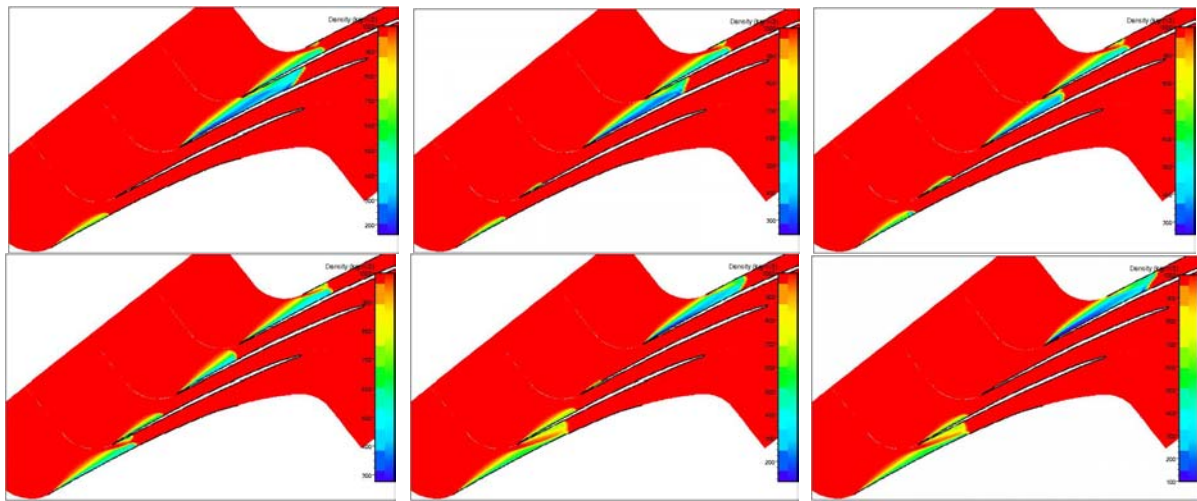


Figure 8.8: Evolution of the Cavitation Sheets.

The sub synchronous instability is characterized by the rotation of a big cavity in reverse direction from the rotation of the inducer.

8.3.2.3 Alternate Configuration

An alternate configuration was obtained for $\sigma_{\text{downstream}} = 0,75$:

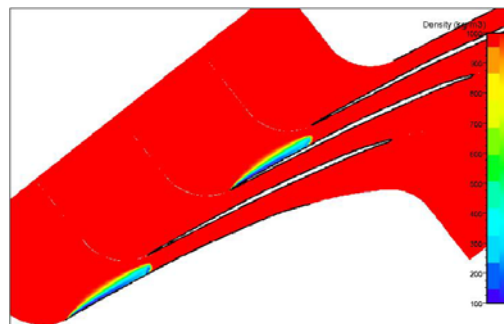


Figure 8.9: Alternate Configuration.

This configuration appeared to be rather unstable as we observed switches from alternate to super synchronous configuration. Another alternate configuration was found for $\sigma_{\text{downstream}} = 0,70$ but this last was unsteady in the relative frame.

8.3.3 Flow Analysis

We devote this last paragraph to the proposal of mechanisms allowing to explain the development of instabilities. We first study the sub synchronous configuration and then the super synchronous configuration.

8.3.3.1 Sub-Synchronous Configuration

The appearance of a sub synchronous configuration is associated to the blockage of a blade to blade channel, which is quite close to the stall phenomenon observed at the inlet of compressors. Thus, it seems

to us that the mechanism explaining the sub synchronous instability may be based on the modification of the incidence at leading edge caused by the fluctuations of mass flow in the channels:

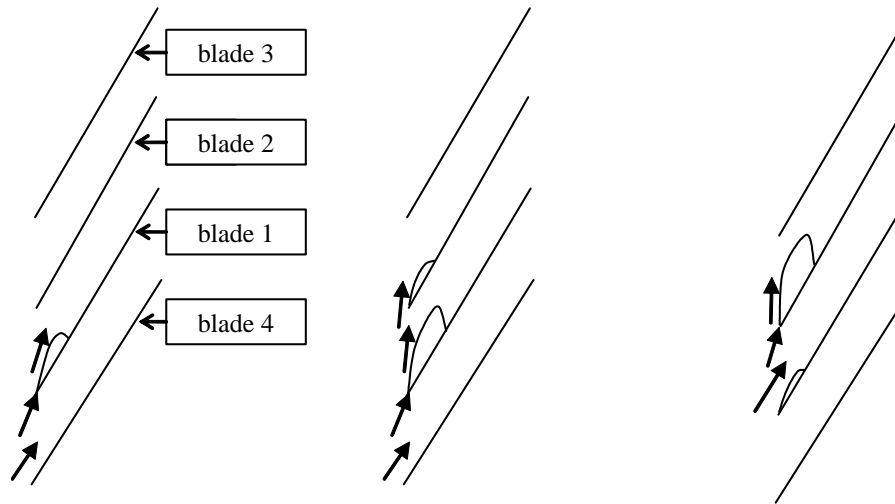


Figure 8.10: Propagation of the Large Cavity (Sub Synchronous Configuration).

The obstruction of a channel by a large cavity causes an increase in the incidence on the upper blade, which deepens the low pressure area on this blade; the direct consequence is an increase of the cavity located on the upper blade. In addition, the mass flow conservation imposes an incidence decrease on the blade below the blocked channel, which tends to decrease the size of its cavity.

8.3.3.2 Super Synchronous Configuration

In order to understand the propagation mechanism of the super synchronous configuration, we use the identification of the blades presented on figure 8.10.

The super synchronous configuration is more complex than the sub synchronous configuration. From our calculations, we propose an original mechanism based on a coupling through the pressure field. Consequently, we observe the evolution of each blade load.

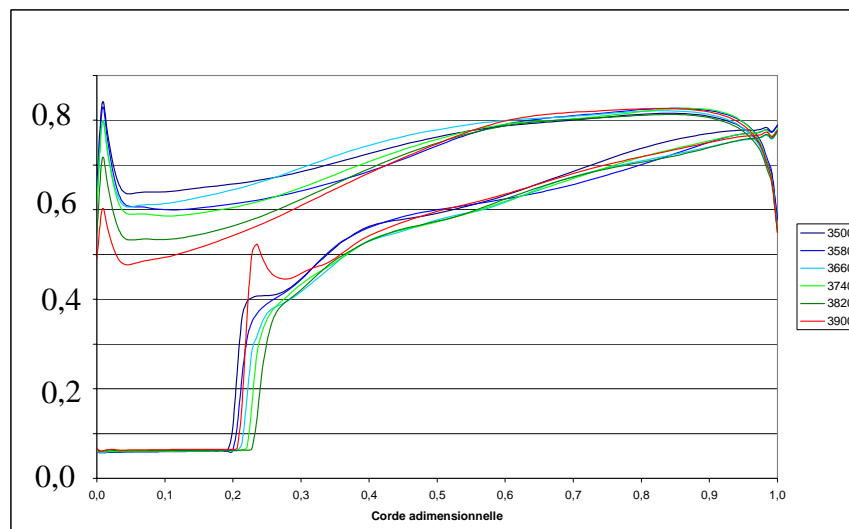


Figure 8.11: Evolution of the Blade 2 Load.

The load of blade 2 is mainly modified on pressure side. Thus, it is noted that the pressure decreases gradually on first half of the blade. This phenomenon occurs whereas the cavity located in the channel located below is growing. This result can be explained by the development of the low pressure area associated with the cavity as it was observed in steady calculations.

The load of blade 3 is mainly modified on suction side due to containment effects (decrease of blade 4 cavity length).

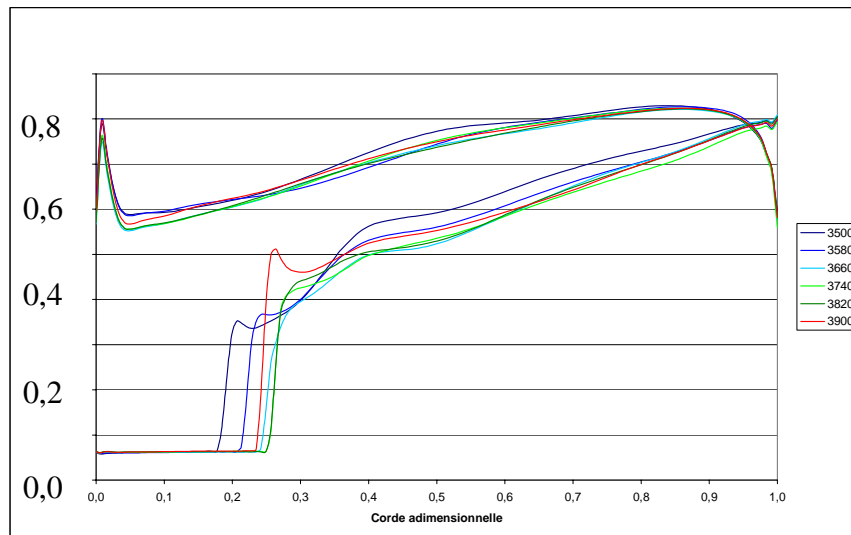


Figure 8.12: Evolution of the Blade 3 Load.

The blades concerned with a fluctuation of cavity length present the most important loading variations as pressure profiles on both sides are modified.

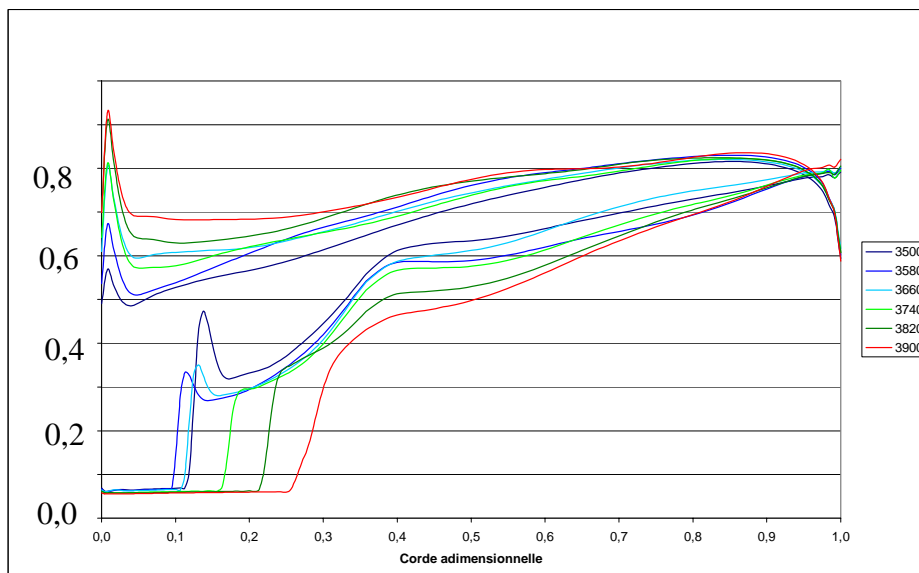


Figure 8.13: Evolution of the Blade 1 Load.

The growth of the cavity on suction side suppresses the brutal pressure rise located in the closure area of the cavitation sheet. On the pressure side, a peak appears near the leading edge which is the signature of an incidence modification. We think that it may cause the decrease of the cavity located on blade 4.

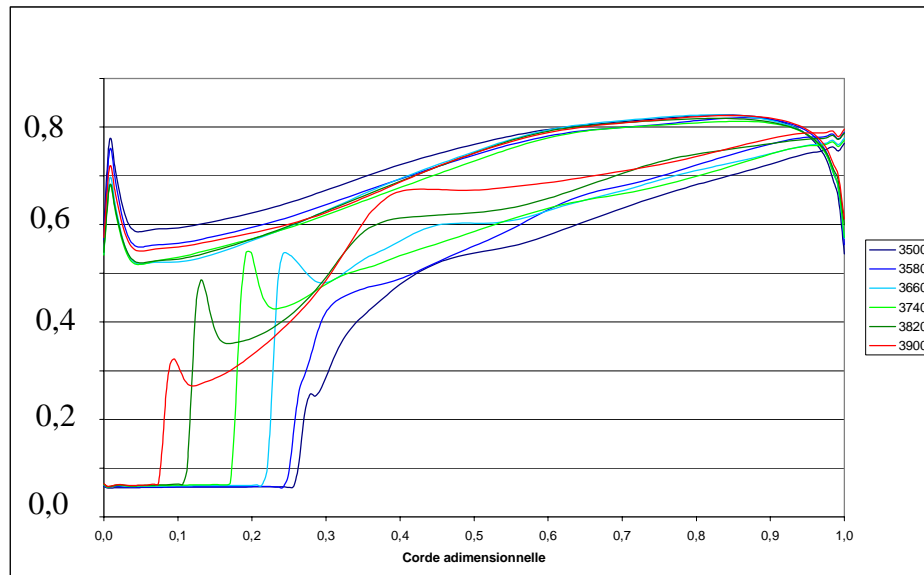


Figure 8.14: Evolution of the Blade 4 Load.

From the analyses of the whole unsteady results, we can propose the following scenario to explain the cavitation super synchronous instability:

- The growth of the cavitation sheet at the blade 1 suction side leads to the increase of the angle of attack of this blade.
- A consequence of this phenomenon is the rise of the pressure at the blade 1 pressure side, near the leading edge.
- The pressure field in the channel 1, located below the blade 1, is modified by this pressure rise, which leads to the decrease of the cavitation sheet attached to the blade 4.
- The presence of the cavitation sheet in the channel 4, located below the blade 4, will change the blade 4 angle of attack, inducing the progressive development of the attached sheet cavitation, and the continuation of the instability propagation.

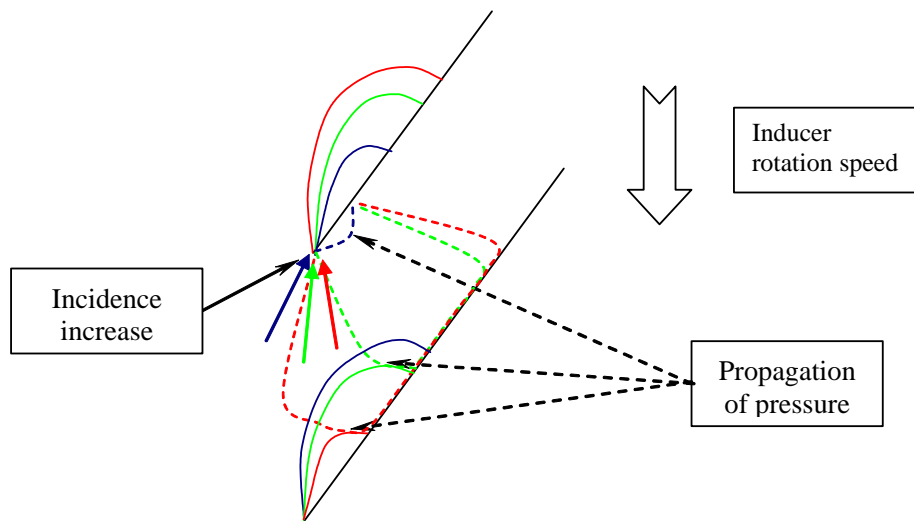


Figure 8.15: Mechanism of the Super Synchronous Configuration.

REFERENCES:

- [1] **Calленаere M., Franc J.P., Michel J.M., Riondet M.,**
The cavitation instability induced by the development of a re-entrant jet. Journal of Fluid Mechanics, vol. 444, p. 223-256, 2001.
- [2] **Combes J.F., Archer A.,**
Etude de la cavitation dans la pompe SHF. 164^{ème} session du Comité Scientifique et Technique de la Société Hydrotechnique de France, EDF Chatou, November 21-22, 2000.
- [3] **Coutier-Delgossa O.,**
Modélisation des écoulements cavitants : étude des comportements instationnaires et application aux turbomachines. PhD thesis INPG, Grenoble, 2001.
- [4] **De Bernardi J.,**
Aspects Expérimentaux et Théoriques des Instabilités de Cavitation dans les Turbopompes de Moteurs Fusée. PhD thesis INPG, Grenoble, 1996.
- [5] **Delannoy Y., Kuény J.L.,**
Two phase flow approach in unsteady cavitation modelling. Cavitation and Multiphase Flow Forum, ASME-FED vol. 98, pp.153-158, 1990.
- [6] **Delhaye J.M., Giot M., Riethmüller M.L.,**
Thermohydraulics of Two phase systems for industrial design and nuclear engineering. Hemisphere Publishing, 1981.
- [7] **Dumont N., Simonin O., Habchi C.,**
Numerical Simulation of cavitating Flows in diesel injectors by a homogeneous equilibrium modelling approach. CAV2001, 4th international symposium on cavitation, Pasadena, California, 2001.
- [8] **Hakimi N.,**
Preconditioning Methods for time dependent Navier-Stokes equations. Ph.D. Thesis, Université Libre de Bruxelles, 1997.
- [9] **Hirsch C.,**
Numerical computation of internal and external flows. Volume 1, John Wiley & Sons, 1988.

- [10] **HIRSCH C.,**
Numerical computation of internal and external flows. Volume 2, John Wiley & Sons, 1990.
- [11] **HORIGUCHI H., WATANABE S., TSUJIMOTO Y., AOKI M.,**
A stability analysis of alternate blade cavitation in inducers. ASME Journal of Fluids Engineering, vol. 122, p. 156-163, 2000.
- [12] **JAMESON A.,**
The Evolution of Computational Methods in Aerodynamics. Journal of Applied Mechanics, vol.50, p. 1052-1070, 1983.
- [13] **KUNZ R. F., BOGER D.A., STINEBRING D. R., CHYCZEWSKI T. S., GIBELING H. J., VENKATESWARAN S., GOVINDAN T.R.,**
A preconditioned Navier-Stokes Method for Two-Phase Flows with application to cavitation prediction. AIAA paper 99-3329, 1999.
- [14] **KUNZ R.F., LINDAU J.W., KADAY T.A., PELTIER L.J.,**
Unsteady RANS and detached eddy simulations of cavitating flow over a hydrofoil. Fifth International Symposium on Cavitation, Osaka, Japan, November 1-4, 2003.
- [15] **POUFFARY B., FORTES-PATELLA R., REBOUD J.L.,**
Numerical Simulation of Cavitating Flow Around a 2D hydrofoil : a barotropic approach. Fifth International Symposium on Cavitation, Osaka, Japan, November 1-4, 2003.
- [16] **POUFFARY B., FORTES-PATELLA R., REBOUD J.L.,**
Unsteady Cavitating Flows in Turbomachinery: Comparison of Numerical Models and Applications. ECCOMAS 2004.
- [17] **QIN Q., SONG C.C.S., ARNDT R.E.A.,**
A virtual single-phase natural cavitation model and its application to Cav2003 hydrofoil. Fifth International Symposium on Cavitation, Osaka, Japan, November 1-4, 2003.
- [18] **REBOUD J-L., STUTZ B., COUTIER O.,**
Two phase flow structure of cavitation: experiment and modeling of unsteady effects. Proceedings of the 3rd Int. Symp. on Cavitation, Grenoble, France, 1998.
- [19] **SOMMERFELD M.,**
Theoretical and Experimental Modelling of Particulate Flows. Von Karman Institute lecture Series, April 3-4, 2000.
- [20] **STUTZ B., REBOUD J.L.,**
Two-phase flow structure of sheet cavitation. Phys. Fluids, vol.9, n°12, pp. 3678-3686, 1997.
- [21] **TSUJIMOTO Y., KAMIJO K., YOSHIDA Y.,**
A theoretical analysis of rotating cavitation inducers. ASME Journal of Fluids Engineering, vol. 115, p. 135-141, 1993.
- [22] **TURKEL E.,**
Preconditioning Methods for solving the incompressible and low speed compressible equations. Journal of Computational Physics, vol. 72, p. 277-298, 1987.
- [23] **WATANABE S., FURUKAWA A., HORIGUCHI H., FUKUTOMI J., TSUJIMOTO Y.,**
Theoretical analysis of unsteady blade loading of inducers under rotating cavitation. CAV2001, 4th international symposium on cavitation, Pasadena, California, 2001.
- [24] **WILCOX D.C.,**
Turbulence Modelling for CFD. DCW Industries, 1993.